Shahrood University of Technology

Journal of Mining and Environment (JME)

Journal homepage: www.jme.shahroodut.ac.ir

Iranian Society of Mining Engineering (IRSME)

Safety Assessment of Earth Dam Using Back-Analysis with the Case Study of Karkheh Dam

Mohammad Salehinik[1], and Hassan Sarfaraz[2*]

1. School of Civil Engineering, Faculty of Engineering, University of Tehran, Tehran, Iran
2. School of Mining Engineering, Faculty of Engineering, University of Tehran, Tehran, Iran

Article Info

Received 25 April 2026
Received in Revised form 30 September 2026
Accepted 6 October 2026
Published online 6 October 2026

DOI: 10.22044/jme.2026.17639.3504

Keywords

Back-Analysis
Dam Safety
Instrumentation
Karkheh Dam
Numerical Modeling

Abstract

Karkheh Dam, a 127-meter-tall earthfill dam with a central clay core in Iran, impounds the country's largest reservoir with a capacity of 5.9 billion cubic meters (BCM). In April 2019, the reservoir experienced an unprecedented water level rise of 5 meters above its normal operating level, raising concerns regarding the dam's long-term stability under sustained high-water conditions. To address these concerns, a comprehensive safety evaluation was conducted, integrating instrumentation data analysis, limit equilibrium analyses using SLOPE/W, and numerical back-analysis alongside nonlinear dynamic simulations utilizing Fast Lagrangian Analysis of Continua (FLAC) software with updated site-specific earthquake records. The numerical model was iteratively calibrated against observed deformations and pore water pressures to ensure appropriate representation of the dam's behavior. While this methodology provides practical approximations for intermediate reservoir levels, statistical evaluations indicate that predictions at the normal water level 220 meters above sea level (m.a.s.l.) carry higher uncertainty and a lower confidence level. Nonetheless, within the limitations of this simplified framework, the results indicate that the dam maintains satisfactory stability under the investigated static and seismic loading scenarios. Under the Maximum Credible Earthquake (MCE), the analysis predicts a maximum residual displacement of approximately 1.35 m. Given the dam's substantial freeboard of 14 m, this deformation indicates a minimal risk of overtopping. Furthermore, the analysis confirms that the upstream and downstream filter zones (5–6 m wide) retain sufficient residual width to prevent internal erosion following seismic deformation. Consequently, within the limitations and assumptions of the adopted numerical framework, no evidence of global instability or overtopping was identified for the investigated loading scenarios.

1. Introduction

The safety and stability assessment of earth and rockfill dams requires a comprehensive understanding of their mechanical behavior under complex loading conditions, including both construction phases and dynamic events. Due to the inherent complexities of earth and rockfill materials, evaluating dam performance relies heavily on advanced numerical modeling techniques. These models are essential for predicting critical responses, such as pore water pressure generation during construction and seismic stability during operation [1,2]. In a broader context, recent advancements in numerical simulations have proven highly effective in analyzing complex geomechanical behaviors, such as hydraulic fracturing and crack propagation patterns, which significantly influence the overall stability of dams and associated underground structures [3,4]. However, the accuracy of such numerical predictions fundamentally depends on the appropriate selection and calibration of constitutive models and material parameters.

Consistent with previous studies, back analysis is a critical methodology for resolving discrepancies between numerical predictions and instrumentation data by utilizing monitoring results

Corresponding author: hamzaban@sut.ac.ir (H. Sarfaraz)

to calibrate material parameters and refine the model [5,6]. Rashidi and Haeri [7] evaluated the behavior of earth and rockfill dams during construction and initial impounding using instrumentation data and numerical modeling, demonstrating that integrating monitoring data with numerical analysis provides a superior understanding of actual dam behavior. Su et al. [8] presented a method for selecting optimal sources in back analysis for multiple material parameters of dams and their foundations. Jeon and Yang [9] developed a back analysis algorithm using FLAC software that has found widespread application in geotechnical projects.

Monitoring and deformation assessment constitute essential components of dam safety management, with both traditional instrumentation systems and modern remote sensing techniques playing vital roles. Integrating monitoring data with numerical models offers a comprehensive framework for predicting potential failure modes and ensuring long-term safety [10]. In line with this perspective, Ghiasi et al. [11] highlighted that comparing monitoring results with numerical modeling not only validates analytical outcomes but also provides a robust basis for conducting back analysis to obtain accurate geotechnical parameters, as demonstrated in the case of the Rudbar embankment dam. Furthermore, the integration of advanced 3D numerical tools, such as PLAXIS 3D and FLAC3D, with in-situ monitoring has become an essential approach for evaluating the stability of complex excavations and supporting infrastructure in dam projects, including the performance of internal pressure tunnels [12,13]. In this context, the Ikizdere Dam was analyzed using the PLAXIS 2D finite element program, and the computed displacements and pore water pressures were compared with monitoring data, demonstrating that properly calibrated numerical models can reliably reproduce the observed behavior of rockfill dams throughout their service life [14]. However, traditional numerical and empirical models often face computational challenges and struggle to fully capture the highly nonlinear and complex behaviors of earth and rockfill dams. Consequently, artificial intelligence (AI) models have emerged as a promising solution for computer-aided back analysis and parameter calibration. Recent advancements demonstrate that AI approaches—such as deep learning, ensemble algorithms, and particularly hybrid models—significantly improve prediction accuracy for complex phenomena like seepage and deformation. By integrating AI with traditional numerical tools, engineers can effectively handle nonlinear behaviors and reduce computational demands, provided that challenges regarding data availability and model generalizability are adequately addressed [15]. For instance, conventional methods for parameter extraction, such as laboratory tests, are often influenced by environmental factors and scale effects. Consequently, the derived parameters may not accurately reflect the true physical properties of the dam. To address this limitation, an Adaptive Cloud Transformation algorithm combined with an RBF neural network has been utilized in recent studies. The resulting acceleration time histories, response spectra, and Fourier amplitudes at the dam's measurement points demonstrated excellent agreement with actual measured values, thereby confirming the rationality and validity of the inversion model. This approach significantly enhances the efficiency of back analysis techniques [16]. However, while these advanced AI and optimization techniques offer high accuracy, they typically require extensive datasets for model training, complex programming, and significant computational overhead. This complexity often limits their practical application for rapid, routine engineering assessments of large-scale embankment dams.

Beyond static performance assessment, seismic stability represents another critical dimension of dam safety assessment, particularly for earth and rockfill dams located in seismically active regions [17]. To address this, recent studies have developed practical relationships to estimate seismic slope displacements based on key parameters such as earthquake magnitude (M_w), yield acceleration ratio (a_y/a_{max}), and fundamental period ratio (T_d/T_p), successfully validating these empirical approaches through finite element modeling [18]. Evaluating the dynamic response of these massive structures requires robust numerical modeling to capture transient changes in pore water pressure and effective stress redistributions. As demonstrated in recent literature, integrating fully coupled hydro-mechanical formulations with advanced constitutive models and utilizing centrifuge test results to calibrate the hydro-mechanical models allows for a more realistic estimation of seismic deformations [19-21]. This coupled approach is particularly critical for aging zoned earth dams, where construction materials and mechanical properties may progressively evolve over decades of operation. Recent comprehensive evaluations of such long-serving structures highlight that ensuring seismic safety

requires a synergistic methodology. By combining pseudo-dynamic analyses—to evaluate dislocation along potential sliding surfaces—with fully coupled elastoplastic continuum models, engineers can deeply investigate internal core stresses, assess the susceptibility to hydraulic fracturing, and verify the overall watertightness integrity of the dam under dynamic loads [22]. Hydro-mechanical coupling is of great significance for high-permeability materials, so much so that for a rockfill dam, accounting for this coupling is vital to prevent overestimating the seismic response [19]. Consequently, numerical models initially calibrated through rigorous static back-analysis provide a reliable foundation for subsequent complex dynamic and seismic evaluations.

Building on this background and motivated by the unprecedented reservoir level rise during the 2019 flood event at the Karkheh Dam, where the water level exceeded the normal operating level by 5 meters, this study presents a comprehensive safety reassessment conducted after 25 years of operation. While previous seismic studies on large embankment dams often rely on computationally expensive and complex optimization algorithms for parameter calibration, this study introduces a streamlined, fast, and efficient back-analysis approach. In this practical methodology, the strength and deformation parameters of the embankment materials are strategically adjusted so that the maximum predicted pore water pressure and dam body settlement match the corresponding in situ instrumentation readings, specifically at the end of the construction stage. This methodology follows an approach analogous to that adopted in the Maroon Dam project [23], but extends its application as a rapid framework for ongoing safety evaluations. These calibrated parameters are subsequently employed to simulate the dam's response under previously unexperienced extreme conditions, namely, dynamic loading during updated seismic events, at two different reservoir levels. This study integrates recent site-specific seismotectonic data with both limit equilibrium methods and hydro-mechanical (volumetric–pore water pressure coupled) finite difference stress-strain modeling. By doing so, it addresses a critical gap in the rapid and reliable safety assessment of aging dams, providing an enhanced and practical framework for their long-term safety management.

2. The Karkheh Dam Characteristics

The Karkheh Dam is a major embankment dam situated in the northwestern province of Khuzestan, Iran. The dam stands 127 meters high, with a crest length of 3,030 meters and a base width of 1,100 meters. Construction was completed on March 24, 2001. The reservoir maintains a normal water level of 220 meters above sea level (m.a.s.l.), providing a storage capacity of approximately 5,900 million cubic meters (MCM). In terms of discharge volume, the Karkheh River ranks third nationally, following the Karun and Dez Rivers in Iran. The dam is founded on conglomerate layers that overlie nearly horizontal mudstone strata at varying elevations within the foundation, as illustrated in Figure 1, which presents the typical cross-section of the Karkheh embankment.

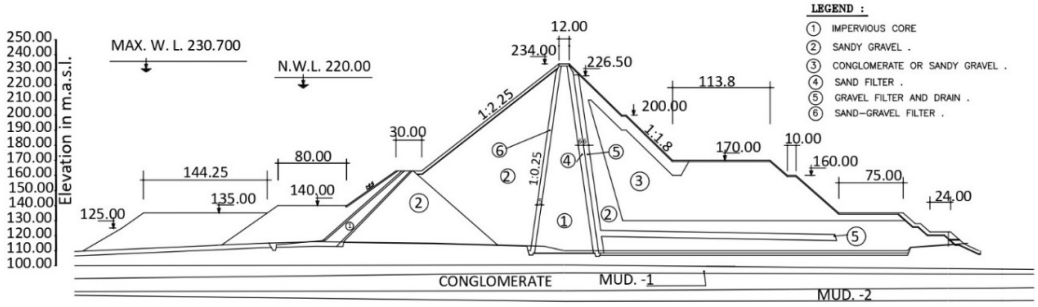

Figure 1. Cross-section of the Karkheh Embankment Dam at its maximum height.

2.1. Instrumentation System and Data Quality

The dam's comprehensive instrumentation system includes 305 vibrating wire electric piezometers, 136 standpipe (Casagrande) piezometers, 505 electric total pressure cells, 31 inclinometers, several survey stations, multiple seepage collection and measurement systems, 111 joint meters, and 180 observation wells. These instruments are distributed across nineteen monitoring sections. This study primarily focuses on data obtained from the central instrumentation section (designated as Section 5), located at the point of maximum dam height (Figure 2), as it is

considered the most critical cross-section of the Karkheh Dam regarding pore water pressure accumulation and maximum settlement. Within this section of the dam body, 6 standpipe piezometers, 27 electric piezometers, and 4 settlement gauges are installed. The definitions of the abbreviations presented in Figure 2 are also provided in Table 1.

The spatial distribution of instruments in the central section is designed to capture the hydraulic and mechanical behavior across critical zones. The 27 electric piezometers and the 6 standpipe piezometers in the dam body are arranged in five specific elevation tiers within the clay core and the upstream/downstream filters to effectively monitor pore water pressure development and dissipation. Regarding deformation monitoring, combined inclinometer-settlement gauges are utilized. These instruments are installed vertically at four distinct locations to profile internal movements: one along the central axis of the core, one within the upstream shell, and two within the downstream shell. A comparable instrumentation layout is adopted for the remaining 18 cross-sections, with the number of instrumentation levels decreasing from five to one in the cross-sections near the dam abutments. Collectively, these 19 monitoring sections are distributed along the longitudinal axis, effectively covering the entire 3,030-meter crest length of the Karkheh Dam.

The long-term performance and data reliability of the Karkheh Dam instrumentation system have been continuously monitored from May 2000 to the present. A comprehensive breakdown of the instruments' current operational status is presented in Table 1. This table details the number of healthy, anomalous, and defective units, alongside the specific defect rate (percentage) and the regular reading frequency assigned to each instrument type. In addition to the requirement for the specialized instrumentation contractor to provide calibration certificates for all electrical systems before the initial readings, portable and centralized readout units undergo periodic calibration during both the construction and operational phases at intervals ranging from six months to a maximum of one year.

Regarding the maximum cross-section (Section 5) utilized in this study, out of a total of 33 electrical and standpipe piezometers installed within the dam body, approximately 57% remain operational; specifically, 30% of the standpipe piezometers and 67% of the electrical piezometers are healthy. For this reason, the back-analysis performed in this research utilizes the readings of the vibrating wire electrical piezometers installed in the dam body.

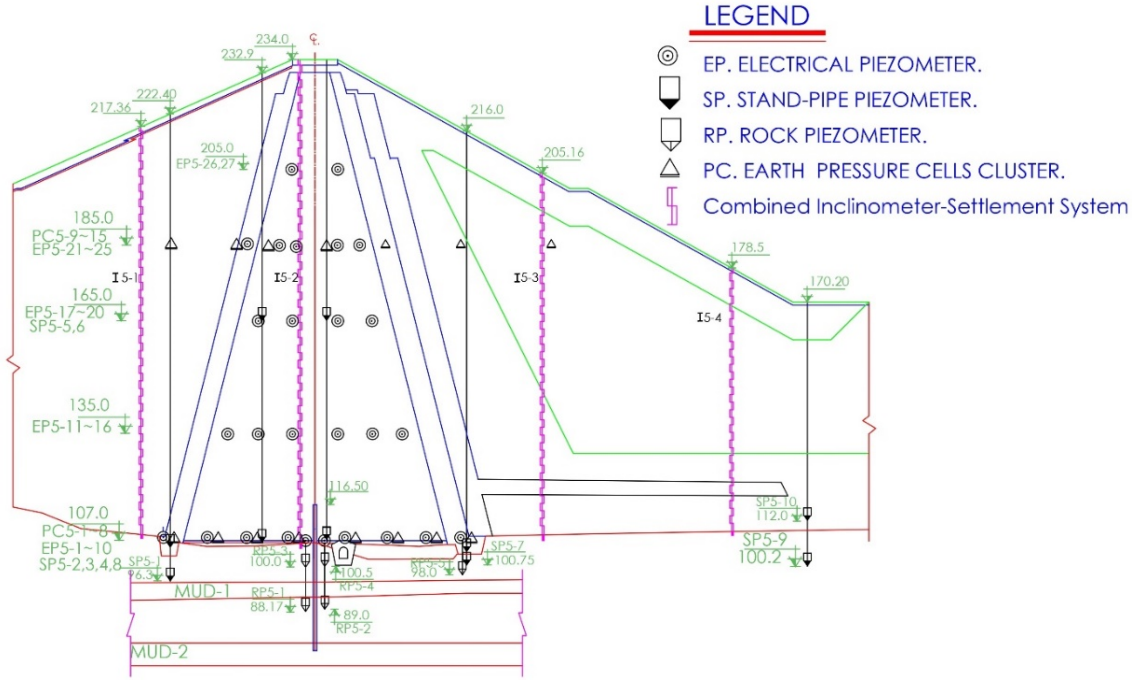

Figure 2. Instrumentation layout at the maximum cross-section of the Karkheh Embankment Dam.

Table 1. Operational status and reading frequency of the monitoring instruments at the Karkheh Dam (2000–Present).

Instrument Type	Abbreviation	Total Installed	Healthy	Anomalous	Defective	Defective Rate (%)	Reading Frequency
Embankment Electrical Piezometer	EP	194	117	30	47	24.2	Daily
Rock Electrical Piezometer	RP	111	25	24	62	55.9	Daily
Pressure cell	PC	505	412	-	93	18.4	Daily
Standpipe Piezometer	SP	136	57	40	39	28.7	Weekly
Observation Well	OW	180	134	21	25	13.9	Weekly
Settlement Gauge	I	28	21	-	7	25	Monthly
Inclinometer	INC	31	19	-	12	38.7	Every two months
Jointmeter	JM	111	107	-	4	3.6	Monthly

2.2. Foundation Conditions and Site Characterization

The rock units in the vicinity of the dam and its abutments are conglomeratic units of the Bakhtiari formation, which also contain claystone interbeds. The site conditions in the seismic hazard analysis are considered in the form of the Vs_30 parameter (the average shear wave velocity in the upper 30 meters of the subsurface profile at the site). Using the acquired geophysical data, the dam foundation is considered to be of rock type with an average shear wave velocity of 900 m/s in the upper 30 meters (Report of Seismic Geophysical Studies at the Karkheh Dam Site, January 1996). Table 2 presents the coordinates of the boreholes in which downhole tests were performed, and the average shear wave velocity was calculated. Additionally, the location of these boreholes is shown in Figure 3. According to the American Society of Civil Engineers (ASCE 7-16), a shear wave velocity exceeding 760 m/s is classified as seismic bedrock (Site Class B) [24].

Table 2. Downhole shear wave velocity (Vs_30) measurements across foundation boreholes (Coordinates: UTM Zone 39N, WGS84).

Borehole	Coordinate		Vs_30 (m/s)
	x	y	
K206	229288.0	3598361.1	989
K205-k224	229454.7	3598407.0	896
K218	229979.7	3598322.0	771
K216-k223	230228.7	3598412.0	1086
K215	230258.7	3598544.5	1050
K201	230414.7	3598479.0	863



Figure 3. Plan view of the dam showing the locations of boreholes used for downhole shear wave velocity testing.

The strength properties of the constituent materials of the dam foundation rock are presented in Table 3, as documented in the original dam study reports, which were derived from shear strength tests performed on samples extracted from the dam foundation.

Table 3. Geomechanical parameters of the dam foundation rock mass

zone	C (kPa)	Φ (^{0})	γ (kN/m^3)
Medium Conglomerate	100	34	22.5
Mudstones	700	24	20

3. Constitutive Modeling Approach and Seismic Degradation Assessment

Before detailing the specific constitutive equations, it is essential to justify the selection of the modeling framework regarding dynamic pore pressure generation and cyclic degradation. While explicit effective stress constitutive models incorporating undrained cyclic response (e.g., PM4Sand or Finn model) are standard for evaluating liquefaction susceptibility in loose saturated sands, recent benchmarking studies on large earth and rockfill dams have highlighted their limitations when applied to dense rockfill shells and cohesive clay cores. For instance, a comprehensive seismic back analysis of the El Infiernillo dam demonstrated that the Strain Hardening/Softening (H/S) model provided a more accurate and reliable prediction of the magnitude and distribution of final permanent displacements when compared directly to field measurements [25].

Conversely, the PM4Sand model consistently predicted extensive permanent deformation. This behavior is attributed to the model simulating excessive cyclic mobility or liquefaction effects in the granular zones, likely due to an overprediction of strain-accumulation potential under the high confining stresses of the rockfill. These findings strongly support the use of meticulously calibrated total-stress models, such as the H/S model, for reliable prediction of safety-critical metrics in high-stress rockfill dams. While the extensive deformation predictions of effective stress models lead to an overly conservative assessment of seismic risk, such an unrealistic degree of conservatism can result in unnecessary and expensive remediation measures.

For well compacted clay cores and filter zones under Maximum Credible Earthquake (MCE) loading, classic flow liquefaction is generally not the governing failure mechanism. Instead, the primary safety concerns are cyclic softening and the accumulation of permanent strains. In the present study, rather than explicitly tracking cyclic pore pressure generation, which lacks reliable calibration data for dense non-liquefiable materials, the macroscopic phenomenological effects of seismic loading such as cyclic degradation and strain accumulation are implicitly captured using the Strain Hardening and Softening model. As demonstrated in benchmarking literature [25], this model reliably evaluates cyclic softening by dynamically updating and reducing the strength parameters of the soil, including cohesion, friction, and dilation as a function of the accumulated plastic shear strain during strong shaking. This approach provides a robust assessment of cyclic degradation without the theoretical over-conservatism associated with explicit liquefaction models applied to non-susceptible zones. Nevertheless, it is crucial to distinguish between pore-pressure variations arising from general hydro-mechanical coupling (i.e., volumetric deformations) and the accumulation of excess pore pressure driven by undrained cyclic soil behavior. It is acknowledged that the present H/S model may not possess the capability to reproduce dynamic pore-water pressures as accurately as other dedicated effective-stress cyclic constitutive models introduced for this purpose. Consequently, this inherent limitation introduces a degree of uncertainty, affecting the overall confidence level of the dynamic predictions regarding detailed transient pore-pressure responses during strong seismic events. Therefore, it must be explicitly noted that liquefaction susceptibility was not independently evaluated or quantified in this study, and the analyses remain strictly limited to the evaluation of permanent deformation and cyclic strength degradation within the constraints of the selected constitutive framework.

3.1. Constitutive Equations

Simple constitutive models involve a limited set of parameters, which simplifies the trial-and-error procedure during back-analysis by allowing more straightforward parameter calibration. In the stress–strain analysis conducted for the back-analysis, the Strain-Hardening/Softening Model was employed, while the Mohr–Coulomb model

was applied in the limit equilibrium slope stability analysis using parameters derived from the back-analysis.

The Strain-Hardening/Softening model is based on the FLAC Mohr-Coulomb model with non-associated shear and associated tension flow rules. The difference, however, lies in the possibility that the cohesion, friction, dilation, and tensile strength may harden or soften after the onset of plastic yield [26]. Subsequently, numerous studies have employed such models for the numerical modeling of earth dams due to their reliability in capturing complex soil responses, such as the stress-dependent stiffness of the rockfill shell and the nonlinear shear behavior of the clay core [27-29].

In the Mohr-Coulomb model, those properties are assumed to remain constant. Here, the user can define the cohesion, friction, and dilation as piecewise-linear functions of a hardening parameter measuring the plastic shear strain. A piecewise-linear softening law for the tensile strength can also be prescribed in terms of another hardening parameter measuring the plastic tensile strain.

To define Hardening/Softening Parameters, plastic shear strain is measured by the shear hardening parameter e^{ps}, whose incremental form is defined as Equation 1.

$$\Delta e^{ps} = \left\{\frac{1}{2}\left(\Delta e_1^{ps} - \Delta e_m^{ps}\right)^2 + \frac{1}{2}\left(\Delta e_m^{ps}\right)^2 + \frac{1}{2}\left(\Delta e_3^{ps} - \Delta e_m^{ps}\right)^2\right\}^{\frac{1}{2}} \quad (1)$$

Where

$$\Delta e_m^{ps} = \frac{1}{3}\left(\Delta e_1^{ps} + \Delta e_3^{ps}\right) \quad (2)$$

and $\Delta e_j^{ps}, j = 1,3$ are the principal plastic shear strain increments.

The tensile hardening parameter e^{pt} measures the accumulated tensile plastic strain; its increment is defined as:

$$\Delta e^{pt} = \Delta e_3^{pt} \quad (3)$$

where Δe_3^{pt} is the increment of tensile plastic strain in the direction of the major principal stress.

The yield function, potential functions, plastic flow rules, and stress corrections are identical to those of the Mohr-Coulomb model, as discussed below.

The failure envelope for this model corresponds to a Mohr-Coulomb criterion (shear yield function) with tension cutoff (tensile yield function). The shear flow rule is non-associated, and the tensile flow rule is associated.

3.1.1. Incremental Elastic Law

In the FLAC implementation of this model, the principal stresses $\sigma_1, \sigma_2, \sigma_3$ are utilized, where the out-of-plane stress σ_{zz} is recognized as one of them. The principal stresses and their corresponding directions are evaluated from the stress tensor components and ordered such that (recalling that compressive stresses are considered negative):

$$\sigma_1 \le \sigma_2 \le \sigma_3 \quad (4)$$

The corresponding principal strain increments $\Delta e_1, \Delta e_2, \Delta e_3$ are decomposed as follows:

$$\Delta e_i = \Delta e_i^e + \Delta e_i^p \qquad i = 1,3 \quad (5)$$

where the superscripts e and p refer to elastic and plastic parts, respectively, and the plastic components are non-zero only during plastic flow. The incremental expression of Hooke's law in terms of principal stress and strain has the form of Equation 6.

$$\begin{aligned}\Delta\sigma_1 &= \alpha_1 \Delta e_1^e + \alpha_2(\Delta e_2^e + \Delta e_3^e)\\ \Delta\sigma_2 &= \alpha_1 \Delta e_2^e + \alpha_2(\Delta e_1^e + \Delta e_3^e)\\ \Delta\sigma_3 &= \alpha_1 \Delta e_3^e + \alpha_2(\Delta e_1^e + \Delta e_2^e)\end{aligned} \quad (6)$$

Where $\alpha_1 = K + 4\frac{G}{3}$ and $\alpha_2 = K - 2\frac{G}{3}$; K and G are the bulk and shear modulus, respectively.

3.1.2. Yield and Potential Functions

With the ordering convention of Equation 4, the failure criterion may be represented in the plane(σ_1, σ_3), as illustrated in Figure 4.

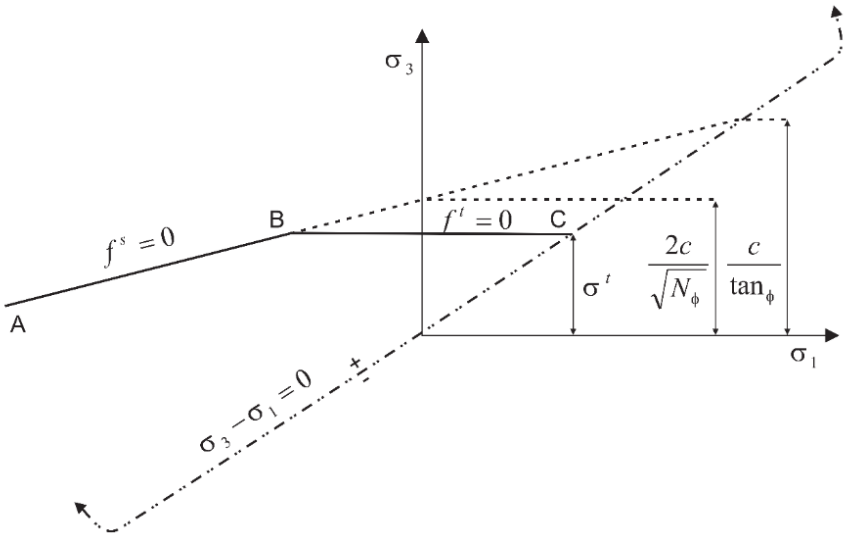

Figure 4. Mohr-Coulomb failure criterion in FLAC.

The failure envelope is defined from point A to point B by the Mohr-Coulomb yield function of the form of Equation 7**:**

$$f^s = \sigma_1 - \sigma_3 N_\phi + 2c\sqrt{N_\phi} \quad (7)$$

and from B to C by a tension yield function of the form of Equation 8:

$$f^t = \sigma^t - \sigma_3 \quad (8)$$

Where ϕ is the friction angle, c is the cohesion, σ^t is the tensile strength, and N_ϕ is defined in Equation 9.

$$N_\phi = \frac{1+\sin\phi}{1-\sin\phi} \quad (9)$$

Note that only the major and minor principal stresses are active in the shear yield formulation;

the intermediate principal stress has no effect. For a material with friction $\phi \neq 0$, and the tensile strength of the material cannot exceed the value , σ^t_{max}given by:

$$\sigma^t_{max} = \frac{c}{\tan\phi} \quad (10)$$

The shear potential function g^s corresponds to a non-associated flow rule and has the form of Equation 11.

$$g^s = \sigma_1 - \sigma_3 N_\psi \quad (11)$$

Where ψ is the dilation angle and N_ψ is defined by:

$$N_\psi = \frac{1+\sin\psi}{1-\sin\psi} \quad (12)$$

The associated flow rule for tensile failure is derived from the potential function g^t, with

$$g^t = -\sigma_3 \quad (13)$$

The flow rules for this model are given a unique definition in the vicinity of an edge of the composite yield function in three-dimensional stress space by application of a technique for the case of a shear-tension edge. The details of this technique are described in the FLAC software manual.

4. Dynamic parameters and Inputs

In an ideal elastic material, the shear modulus (G) remains independent of the shear strain level, while the damping ratio (ξ) is consistently zero. In contrast, soils exhibit nonlinear behavior, characterized by progressive variations in both shear modulus and damping ratio as shear strain increases [30,31]. This nonlinear response is particularly pronounced in soils composed of discrete particles. For example, granular soils with negligible fines, such as clean sands, display stronger nonlinear behavior compared to cohesive, fine-grained soils [32].

Several factors influence the shear modulus and damping ratio, including confining pressure, relative density, overconsolidation ratio, soil aging, disturbance, soil type, and stress anisotropy. These parameters can be determined or estimated through field investigations, laboratory experiments (e.g., large-scale cyclic triaxial tests), empirical correlations, and analytical or numerical models.

During the feasibility studies for the Karkheh Dam, large-scale cyclic triaxial tests were

Corresponding author: hamzaban@sut.ac.ir (H. Sarfaraz)

performed on the dam materials. The core and shell materials were examined using samples with diameters of 20 cm and 30 cm, respectively.

The small-strain shear modulus (G_{max}) can be determined through laboratory tests (e.g., cyclic triaxial or resonant column tests), field investigations (e.g., shear wave velocity measurements), or empirical correlations derived from soil properties. In this study, the empirical relationships used to calculate G_{max} (in kPa), as presented in Table 4, were developed based on the mean effective confining stress (σ'_0, in kPa) obtained from static analyses of the dam. To accurately capture the dynamic response of the distinct materials within the dam body, specific empirical correlations were selected for each zone: the Hardin & Black (1968) [33] relationship was adopted for the cohesive clay core to account for the influence of void ratio and plasticity; the Kokusho & Esachi (1981) [34], equation was utilized for the shell, as it is specifically derived for coarse-grained gravels and rockfill, reflecting their higher stiffness compared to the core; and the Seed & Idriss (1970) [35] formulation was applied to the filter and drain zones, representing the standard behavior of cohesionless granular soils. In the latter equation, the parameter k_{2max} represents a shear modulus coefficient that correlates directly with the soil's relative density, typically ranging from 30 for loose sands to 75 for very dense sands. A value of $k_{2max} = 60$ was selected for this study, corresponding to the dense compaction state of the sandy materials in the filter zone. The variation of the normalized shear modulus and damping ratio with increasing shear strain is illustrated in Figure 5.

Table 4. Empirical correlations used to estimate the small-strain shear modulus (G_{max})

Material type	Reference	Equations
core	Hardin & Black(1968) [33]	$G_{max} = \frac{3270(2.97-e)^2}{1+e}(\sigma'_0)^{0.5}$
Filter and drain	Seed & Idriss (1970) [35]	$G_{max} = 220 * k_{2max}(\sigma'_0)^{0.5} \quad k_{2max} = 60$
shell	Kokusho & Esachi (1981) [34]	$G_{max} = \frac{8400(2.97-e)^2}{1+e}(\sigma'_0)^{0.5}$

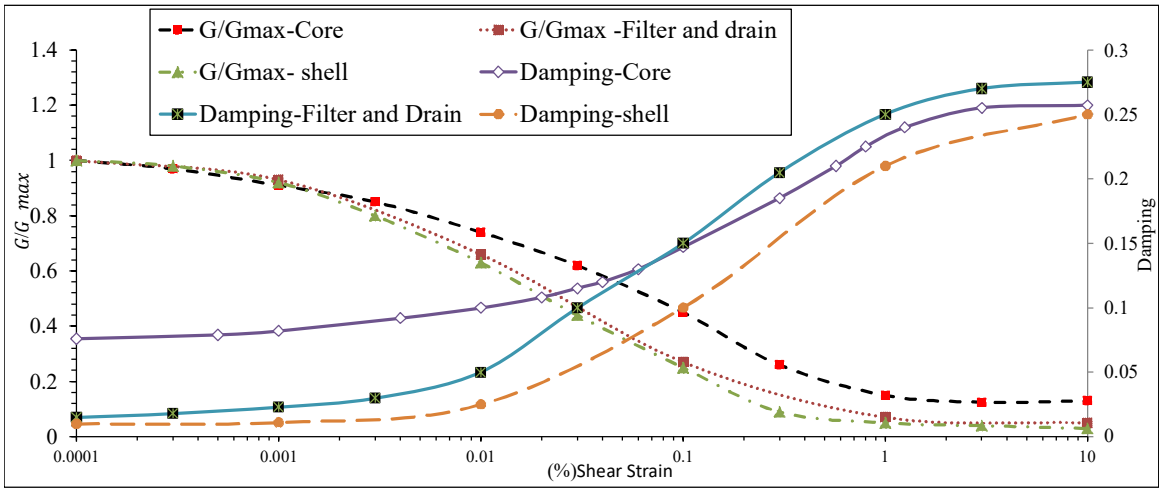

Figure 5. Variation of normalized shear modulus (G/G_{max}) and damping ratio (D) with shear strain (γ) for different constituent materials of the dam body.

The dynamic analysis of the Karkheh Dam necessitated a comprehensive review and update of the site-specific seismotectonic investigations and seismic hazard assessments. A central outcome of these studies is the characterization of strong ground motion, particularly the peak horizontal and vertical acceleration components, which are critical for evaluating the dam's structural stability. The highest level of ground motion considered is the Safety Evaluation Earthquake (SEE), which, for a high-hazard structure like the Karkheh Dam, is defined as the Maximum Credible Earthquake (MCE). Based on the identification of regional seismic sources and in accordance with the International Commission on Large Dams (ICOLD) Bulletin 148 [46], the strong motion parameters for the SEE were defined at the 84th percentile of the MCE distribution. Building upon this framework, several seismic hazard levels were established for the project, considering their

probability of occurrence: the Operational Basis Earthquake (OBE) with a 145-year return period, the Design Basis Earthquake (DBE) with a 475-year return period, the Maximum Design Earthquake (MDE) with a 2,000-year return period, and the aforementioned SEE. The peak ground acceleration values for each of these levels are summarized in Table 5, and the corresponding target response spectrum for the MCE-level horizontal acceleration, with 5% damping, is presented in Figure 6. The response spectra for the 145-year (OBE) and 475-year (DBE) return periods were developed using both probabilistic and statistical methods, with the envelope of the two approaches selected as the target spectrum. The MCE response spectrum was derived using a deterministic method. Considering the significant downstream hazards and based on ICOLD recommendations, the 84th percentile of the MCE distribution was selected for the dynamic analysis.

To conduct the nonlinear dynamic analyses, it was essential to select a suite of ground motion records that are representative of the seismic hazard defined by the target spectrum (Figure 6). The selection process followed a multi-criteria approach, considering key characteristics such as earthquake magnitude, source-to-site distance, fault mechanism, frequency content, significant duration of strong motion, the site's geological conditions, and the Peak Ground Acceleration (PGA) values before and after scaling. After a thorough review of reputable national and international strong-motion databases, an initial set of qualified accelerograms was chosen. These records were then scaled using the spectral matching technique in the time domain to ensure their response spectra were compatible with the target design spectrum.

Spectral matching is a process in which a real or synthetic accelerogram is adjusted so that its response spectrum closely matches a target spectrum over a specified range of periods and for a given damping ratio (typically 5%). This approach is one of the most common and recommended methods for modifying accelerograms because it effectively preserves the fundamental non-stationary characteristics (such as phase content and time-varying intensity) of the original ground motion. The method operates by adding a series of small, controlled wavelet functions to the original time history. These wavelets are localized in time and controlled in frequency, ensuring that the adjustments are precise and minimally invasive.

The general algorithm for this process is as follows:

1. The response spectrum of the initial record is calculated.
2. The mismatch between the calculated spectrum and the target spectrum is determined at various periods.
3. A wavelet function is generated for each period where a significant mismatch exists.
4. These wavelets are gradually and iteratively added to the time history record.
5. The process is repeated until the difference between the record's spectrum and the target spectrum falls within a predefined acceptable tolerance.

During the accelerogram selection process, primary preference was given to records registered in Iran, provided they met the suitability criteria. When appropriate local records were not available, ground motions from other global regions were utilized. The final selection was based on the records showing the best overall consistency with all specified parameters. Consequently, the dynamic analyses at the MCE level were conducted using four scaled ground motions: Bam (2003), Loma Prieta (1989), Sarpol-e Zahab (2017), and Northridge (1994). A summary of these selected accelerograms and their relevant parameters is presented in Table 6. These input motions were appropriately scaled to match the target acceleration response spectrum defined for the site. The L and T components listed in Table 7 represent the two orthogonal horizontal components of the recorded ground motions, corresponding to the longitudinal and transverse directions, respectively. The L and T components were applied separately as alternative horizontal input motions along the horizontal axis of the 2D plane-strain model (corresponding to the upstream–downstream direction of the dam cross-section). The vertical ground-motion component was not included in the numerical analyses. This assumption is consistent with the guidance provided in ICOLD Bulletin 148 [36], according to which the dynamic response of embankment dams generally does not require consideration of the vertical component of ground motion or the hydrodynamic effects of the reservoir water. Although these effects may become relevant for embankment dams with particularly steep slopes, the Karkheh Dam has relatively gentle slopes. Therefore, the vertical ground-motion component was omitted from the present analysis. It should be noted that the reported post-earthquake

residual vertical crest displacement represents the vertical deformation response of the dam induced by the applied horizontal seismic loading and does not indicate that a vertical acceleration component was directly imposed in the model.

The numerical simulations were performed using the explicit Finite Difference Method (FDM) within the FLAC software environment. During the time-history analyses, displacements were monitored at various grid points, and the post-earthquake residual displacement values were determined from the final displacement contours and the corresponding end-of-analysis values recorded in the displacement histories. As evidenced by the displacement patterns (e.g., Figure 16), the maximum deformation consistently occurred at the dam crest; therefore, the post-earthquake residual vertical displacement at the crest was adopted as the criterion for comparing the severity of the different seismic records. To provide a comprehensive assessment of the seismic response and address the inherent variability of ground motions, the results for all four selected MCE accelerograms were evaluated. The statistical parameters including maximum (max), minimum (min), mean (μ) ,and standard deviation (σ) of the predicted responses at the reservoir elevation of 220 m.a.s.l. across the entire suite of records are summarized in Table 7.

Among the considered horizontal input components, the T component of the Sarpol-e Zahab record induced the maximum post-earthquake residual vertical crest displacement. The scaled accelerogram used as the input for this ground motion is illustrated in Figure 7. However, it must be explicitly noted that while this record is defined as the governing case with respect to this specific deformation metric, this does not necessarily imply that it dictates all other aspects of seismic performance, such as localized stress concentrations or internal cracking. Consequently, although statistical bounds are provided for all records, the detailed evaluation of stress distribution and failure zones in the subsequent sections focuses on the Sarpol-e Zahab record to illustrate the structural response under the condition of maximum predicted deformation.

Table 5. Peak horizontal and vertical ground acceleration values at the Karkheh Dam site for different seismic hazard levels, based on the average of applied attenuation relationships.

Design Earthquake	PGA (Mean)	
	PGHA (g)	PGVA (g)
OBE (145yr)	0.145	0.086
DBE (475yr)	0.233	0.132
MDE (2000yr)	0.390	0.211
MCE (50%)	0.356	0.241
MCE (84%)	0.641	0.426

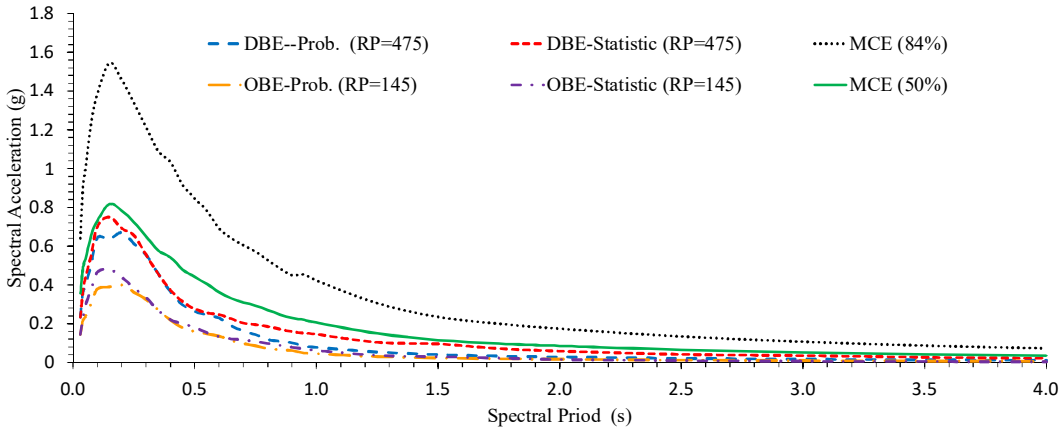

Figure 6. Uniform response spectra of the horizontal component for different return periods (5% damping).

Table 6. Characteristics of the scaled accelerograms selected for the design earthquakes.

Design Earthquake	Event Name	Date	Magnitude	Station	R (Km)	Site Conditions	Focal Mechanism	Significant Duration	Component	Peak(g)
OBE	HAJI ABAD Iran-Fars 2	Jul.10,2003 (17:06)	Mw5.8	Haji Abad	35.0	Soft Rock	R	14.0	L	0.360
								13.7	T	0.294
								18.3	V	0.182
	AHMADI Iran-Hormozgan 2	Mar.05, 2000 (09:40)	Mw5.4	Ahmadi	13.0	Type: II	R	6.7	L	0.134
								5.6	T	0.207
								7.6	V	0.106
	SEYMAREH Iran-Ilam 1	Oct.04,1998 (00:42)	Mw5.3	Seymareh Dam	8.0	Type: I Hard Rock	RS	1.3	L	0.386
								1.3	T	0.278
								1.4	V	0.454
	QESHM Iran-Hormozgan 1	Nov.27,2005 (10:22)	Mw6.0	Souza	17.0	Type: I-II	R	7.4	L	0.331
								7.4	T	0.221
								12.4	V	0.118
DBE	KAREBASS Iran-Fars 2	May 06,1999 (23:00)	Mw6.2	Dehbala	24.0	Type: I	SS	7.0	L	0.326
								8.2	T	0.353
								9.1	V	0.238
	Mormori Iran-Ilam 1	Aug18,2014 (02:32)	Mw6.0	Abdanan	30.0	Type: II	R	5.6	L	0.218
								6.0	T	0.2
								9.8	V	0.1
	SILAKHOR Iran-Lorestan 2	Mar.31,2006 (01:17)	Mw5.9	Darreh Asbar	27.0	Type: I	SS	13.1	L	0.108
								13.4	T	0.126
								15.0	V	0.07
	Sar Pol Zahab Iran-Kermanshah 2	Nov.25,2001 (16:37)	Mw6.3	Qasr Shirin	24.0	Type: III	SS	12.8	L	0.224
								11.4	T	0.243
								12.8	V	0.11
MDE	BOJNURD Iran-Khorasan 2	Feb.04,1997 (10:37)	Mw6.5	Raz (Bakhshdari)	34.0	Type: II	SS	14.5	L	0.08
								13.6	T	0.097
								15.1	V	0.065
	ZARAND Iran-Kerman 1	Feb.22,2005 (02:25)	Mw6.3	Qadrooni Dam(office)	19.0	Type: II	R	13.8	L	0.209
								14.5	T	0.143
								13.8	V	0.103
	AHAR-FRIST Iran-Azarbaijan 1	Aug.11,2012 (12:23)	Mw6.4	Ahar	18.0	Type: II	SS	11.2	L	0.2
								10.5	T	0.282
								13.3	V	0.099
	AVAJ CHANGOOLEH Iran-Qazvin	Jun.22,2002 (02:58)	Mw6.5	Avaj (Bakhshdari)	26	Rock	R	6.0	L	0.453
								6.8	T	0.465
								6.5	V	0.299
MCE/SSE	Bam Iran-Kerman 1	Dec.26,2003 (01:56)	Mw6.5	Bam (Farmandari)	7.0	Type:II_III	SS	7.9	L	0.794
								9.1	T	0.631
								7.4	V	1.01
	LOMA PRIETA USA 8	Oct.18,1989 (00:50)	Mw6.9	Gilroy Array #2	12.7	CWB(D) USGS©	RO	11.0	L	0.367
								9.5	T	0.322
								9.1	V	0.294
	Sar Pol Zahab Iran-Kermanshah 1	Nov.12,2017 (18:18)	Mw7.3	Sarpol-e zahab(SPZ)	39.0	Type:II	TR	10.8	L	0.697
								9.8	T	0.575
								10.5	V	0.389
	NORTHRIDGE USA 11	Jan.17,1994 (12:30)	Mw6.7	Topango Canyon Blvd Canoga Park	6.5	Rock	RN	10.8	L	0.381
								9.8	T	0.343
								10.5	V	0.41

Table 7. Statistical summary (maximum, minimum, mean, and standard deviation) of the predicted seismic responses at a reservoir elevation of 220 m.a.s.l. across the suite of four MCE records.

Seismic Event	Horizontal Displacement (cm)		Vertical Displacement (cm)	
	T Component	L Component	T Component	L Component
Bam (2003)	27.0	30.5	58.0	58.5
Loma Prieta (1989)	29.0	27.5	55.5	55.0
Sarpol-e Zahab (2017)	80.0	32.0	135.0	65.0
Northridge (1994)	26	25.5	45.0	40.0
maximum(max)	80.0	32.0	135.0	65.0
minimum (min)	26.0	25.5	45.0	40.0
mean(μ)	40.5	28.8	73.3	54.6
standard deviation (σ)	26.3	3.0	41.6	10.6

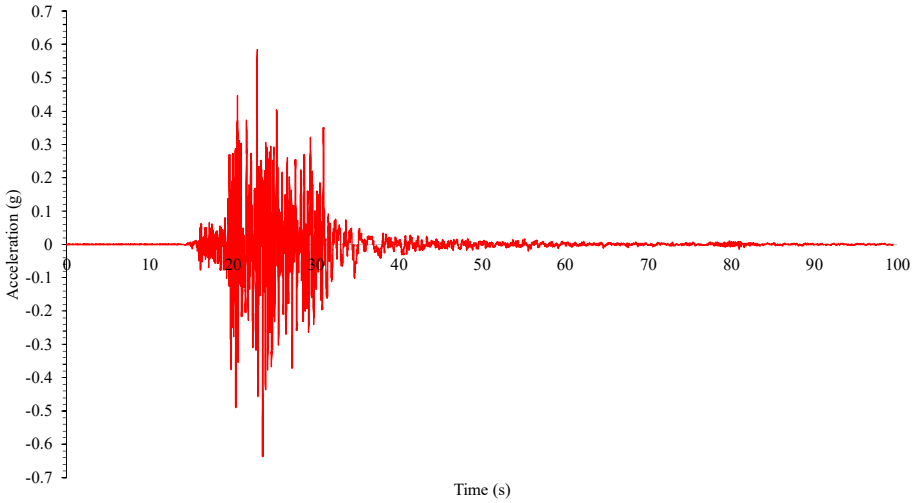

Figure 7. Scaled horizontal acceleration time history of the T-component of the Sarpol-e Zahab earthquake at the MCE level.

5. Hydro-Mechanical Coupling Formulation

To accurately capture the transient changes in pore water pressure and the resulting effective stress redistributions during seismic loading, a fully coupled hydro-mechanical (effective stress) dynamic analysis was performed using the FLAC software [26].

In this coupled numerical approach, the interaction between the solid skeleton and the pore fluid is continuously updated, with fluid flow and mechanical deformation calculations performed simultaneously in each time step. The mechanical behavior of the solid skeleton was simulated using the Strain-Hardening/Softening constitutive model, the details of which are comprehensively discussed in Section 3 of this paper. The mechanical volume changes of the saturated elements under dynamic loading induce changes in pore water pressure, while these generated pore pressures, in turn, directly affect the effective stresses and the subsequent mechanical response of the soil skeleton. It should be noted that this formulation represents volumetric–pore water pressure hydro-mechanical coupling, wherein dynamic pore pressures are governed by instantaneous volumetric strain increments rather than cyclic contractive plastic pore-pressure accumulation (such as in Finn or PM4Sand liquefaction models).

Specifically, in each computational step, the change in pore water pressure (p) is calculated based on the fluid bulk modulus (K_w) and the mechanical volumetric strain of the element. The continuity equation for the fluid, which balances the change in element volume with the net fluid flux, is expressed as:

$$\frac{\partial p}{\partial t} = -\frac{K_w}{nV}\left(\sum Q + \frac{\partial V}{\partial t}\right) \qquad (14)$$

Where n is the porosity, t denotes time, V is the total volume of the node, and Q is the unbalanced fluid flux from surrounding elements, and $\frac{\partial V}{\partial t}$ represents the rate of volume change. For the explicit finite difference scheme used in FLAC, this relationship is solved in the following incremental form to update the pore pressure at each time step:

$$p^{(new)} = p^{(old)} - \frac{K_w}{nV}\left(\sum Q\Delta t + \Delta V_{mech}\right) \quad (15)$$

Where $p^{(new)}$ and $p^{(old)}$ are the pore water pressures at the current (new) and previous (old) timesteps, respectively. ΔV_{mech} represents the mechanical volumetric deformation occurring during the time step Δt. By utilizing this coupled formulation along with the specified constitutive model, the dynamic generation and dissipation of pore water pressure, and their direct impact on the transient stability of the earth-fill dam, were explicitly taken into account throughout the seismic simulations.

To account for partially saturated conditions (e.g., zones above the phreatic surface) and to prevent the unrealistic generation of high negative pore pressures, the numerical scheme employs a strict mass conservation logic. In FLAC, if the computed pore water pressure drops below a user-defined fluid tension limit—assumed to be zero in this study to conservatively neglect matric suction effects—the pressure is capped at zero. Under this condition, the net fluid flux and mechanical volume changes do not alter the pore pressure; instead, they dynamically update the degree of saturation (S). The continuity equation for partially saturated nodes is expressed as:

$$S^{(new)} = S^{(old)} - \frac{\sum Q\Delta t + \Delta V_{mech}}{nV} \quad (16)$$

Where $S^{(new)}$ and $S^{(old)}$ are the degrees of saturation at the current and previous timesteps, respectively. The pore pressure remains at zero as long as the degree of saturation is less than unity $(S < 1)$. If the computed saturation reaches or exceeds 1 during the transient analysis, it is capped at $S = 1$, indicating a return to fully saturated conditions, and the calculation automatically reverts to using Equation 15. This built-in logic ensures that fluid mass is strictly conserved and that the transitions between partially and fully saturated states are accurately modeled throughout the seismic loading phase. Furthermore, this dynamic updating of the degree of saturation feeds back into the fully coupled hydro-mechanical formulation in three primary ways. First, it establishes a mechanical threshold; the fluid phase provides no bulk compressive stiffness to the soil skeleton until full saturation is reached, at which point dynamic excess pore pressure generation is reactivated. Second, the soil bulk density is dynamically adjusted to accurately reflect changes in inertial forces during seismic loading, calculated as:

$$\rho = (\rho_{sat} - \rho_d)S + \rho_d \quad (17)$$

Where ρ is the current bulk density of the soil mass, ρ_{sat} and ρ_d are the saturated and dry soil densities, respectively. Third, the unsaturated flow is governed by scaling the relative permeability $\left(\hat{k}(S)\right)$ using an empirical function of saturation. This ensures a smooth transition of hydraulic conductivity between fully saturated and partially saturated states, which is defined by:

$$\hat{k}(S) = S^2(3 - 2S) \quad (18)$$

6. Back Analysis

A two-dimensional finite difference mesh was developed and utilized for the purpose of back-analysis (as shown in Figure 8). To accurately replicate the actual stress-strain history, the construction phase was simulated stage-by-stage (layer-by-layer) in strict accordance with the real construction schedule. The dam foundation was excluded from the model for two primary reasons. First, field investigations, including shear wave velocity measurements from feasibility study tests as described in section 2.2, confirmed that the seismic bedrock coincides with the dam base. This finding permitted the direct application of earthquake records at the dam base without the need for explicit foundation modeling. Second, construction-induced settlement data were unavailable, as geodetic monitoring points in the foundation gallery were installed only after construction, thereby preventing reliable characterization of the foundation response.

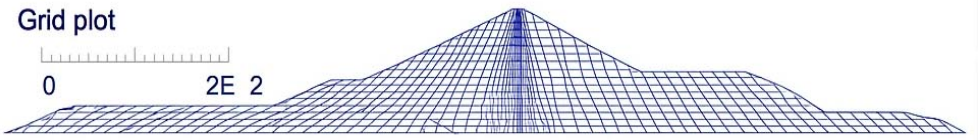

Figure 8. Finite difference mesh used for back-analysis of the Karkheh Dam.

The overall back-analysis procedure was conducted as follows, employing a multi-criteria calibration approach to explicitly mitigate the inherent issue of parameter ambiguity in the solution:

1. Initial Setup: After establishing the geometry of the dam body, the initial estimates for the strength and deformability parameters were extracted from the Phase II Dam Design Study Report and implemented in the model. This step provided a geomechanically realistic baseline to bound the potential solution space and avoid physically meaningless mathematical results.

2. Initial Calibration Target: The pore water pressure and settlement at the end-of-construction (EOC) condition were then read from the model. The procedure involved iteratively modifying the material parameters, keeping them within the initial parameter range, until the maximum predicted pore water pressure and vertical settlement at the end-of-construction exactly matched the values measured by the in situ instrumentation. Requiring the model to simultaneously reproduce two independent physical variables (deformation and hydraulics) significantly constrains the admissible parameter space and reduces parameter ambiguity.

3. Validation Phase (Reservoir Impoundment): Subsequently, the model was evaluated for reservoir impoundment scenarios at two specific water surface elevations: 194 m.a.s.l. and 220 m.a.s.l. This evaluation involved reading the pore water pressures and settlements at the instruments located in the maximum cross-section along the dam's height. These predicted values were then compared against the corresponding measured values at the instrument locations, and the Root Mean Square Error (RMSE) and other error metrics were calculated for these parameters. The comparisons between the measured and numerically modeled pore water pressures and settlements are presented in Tables 8 and 9, respectively. Furthermore, the variations in settlement along the dam's height for the two reservoir water elevations of 194 and 220 m.a.s.l. are illustrated in Figure 13.

4. Final Parameters: Once the model performance was validated spatially across multiple elevations and for dual-variable behaviors, the refined parameters were reported as the final parameters in Table 11. This dual-variable matching approach provides an indicative reference state within the investigated parameter bounds.

5. Forward Analysis: Finally, this calibrated model was utilized for conditions the dam has not yet experienced, specifically for a nonlinear dynamic analysis under the MCE (Maximum Credible Earthquake) loading. It is crucial to emphasize the distinction between static calibration and dynamic validation at this stage. The calibrated parameters were obtained exclusively from static end-of-construction observations. While applying these statically derived parameters to subsequent nonlinear dynamic analyses serves as a practical engineering approximation within the framework of this study, it does not constitute a direct validation of the dynamic constitutive response of the materials under cyclic loading. Nevertheless, initializing the dynamic model with a calibrated static stress state significantly reduces the baseline uncertainties. Therefore, despite the inherent limitations of extrapolating static parameters to dynamic behavior, this forward analysis provides engineering insights into the seismic performance and potential vulnerabilities of the dam under extreme MCE scenarios.

The detailed continuation of the aforementioned procedure is described below:

The calibration procedure employed a systematic parametric calibration approach governed strictly by field instrumentation data. The rationale for parameter selection was robust; the initial parameters were not selected arbitrarily but were directly adopted from the detailed Phase II geotechnical reports. These baseline values, derived from actual shear strength tests conducted on the site materials, provided a reliable and physically meaningful starting point. During the calibration phase, the parameters of the dam body were systematically adjusted around their initial Phase II values. The adjustment bounds were strictly constrained by realistic geotechnical limits for the specific materials, ensuring that the calibrated parameters remained physically sound and consistent with observed material behavior. The stopping criterion for this iterative process was defined as the point at which the numerical model's predictions for both the maximum pore water pressure and the maximum settlement at the end-of-construction precisely matched the actual readings from the field instruments. Once this convergence was achieved, the iterations were halted, and these values were locked as the final parameters for subsequent analyses.

Figure 9 illustrates the settlement profiles along the dam height at various dates. These data correspond to the settlement readings obtained

from the Combined Inclinometer-Settlement System I5-2, which is located in the dam core at maximum cross-section as shown in Figure 2. As evident from this figure, across all dates, the maximum settlement occurs at approximately the mid-height of the dam, reaching a peak value of 120 cm at the end-of-construction on March 27, 2001. Similarly, according to the readings from the electrical vibrating wire piezometers presented in Figure 10, the maximum pore water pressure within the dam core was 695 kPa. The locations of these piezometers are also depicted in Figure 2. This maximum pore water pressure was recorded by electrical piezometer EP5-12, which is located at the lower elevations of the core.

Following the completion of the back-analysis, Figures 11 and 12 present the numerical results for the end-of-construction (EOC) stage, where Figure 11 depicts the pore water pressure contours and Figure 12 illustrates the vertical settlement contours of the dam. The qualitative and quantitative patterns of settlement and pore water pressure variations obtained from the software are fully consistent with the instrumentation readings shown in Figures 9 and 10. Specifically, the numerical analysis indicates that the pore water pressure at the location of piezometer EP5-12 reached 695 kPa, and the maximum vertical settlement at the mid-height of the core was calculated as 120 cm, demonstrating agreement with the field monitoring data. As mentioned earlier, following the evaluation of the model's performance presented in Tables 8 and 9 and Figure 13, the final material parameters were selected according to Table 11.

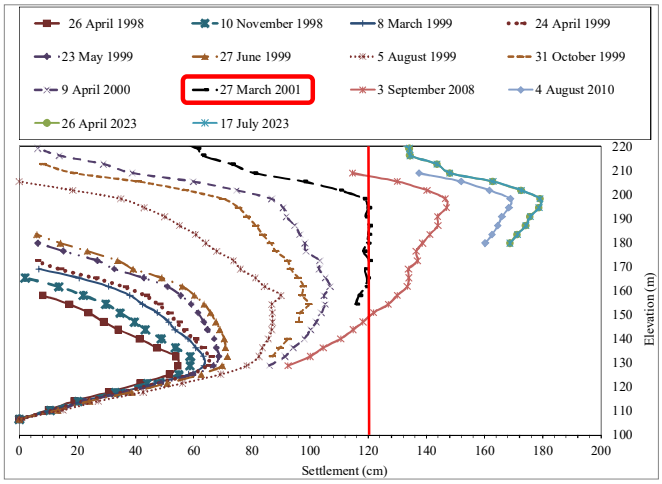

Figure 9. Settlement profiles along the dam height at different times, obtained from the Combined Inclinometer-Settlement System I5-2 installed in the core (location shown in Figure 2). Note that 27 March 2001 corresponds to the end-of-construction (EOC).

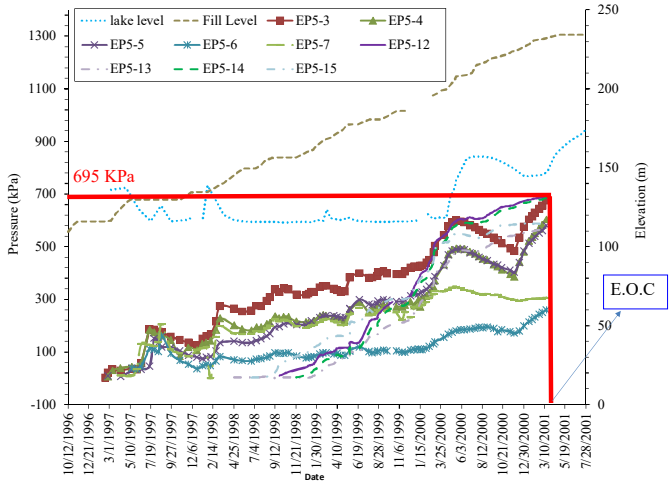

Figure 10. Variations in pore water pressure measured by electrical vibrating wire piezometers installed in the maximum cross-section of the dam, alongside reservoir water level fluctuations (location shown in Figure 2).

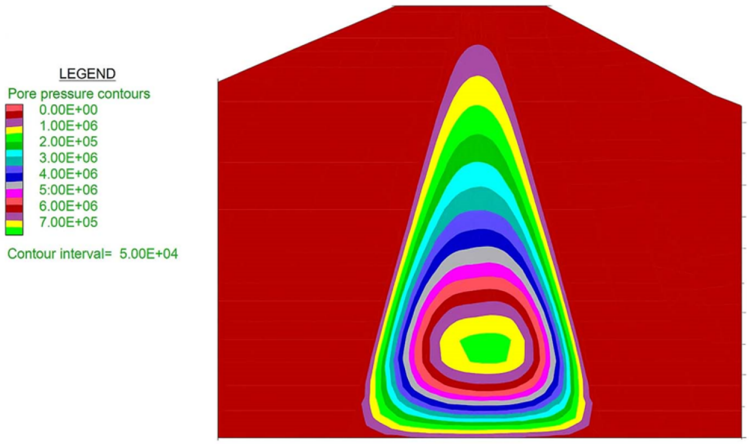

Figure 11. Pore water pressure contours (Pa) in the dam core obtained from back-analysis of the end-of-construction (EOC) stage.

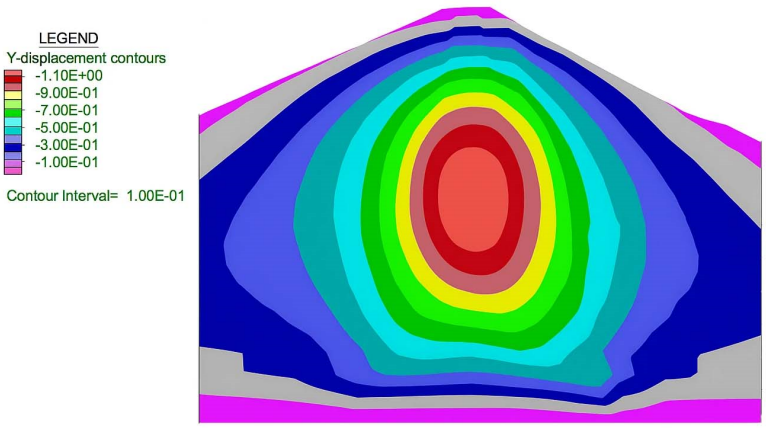

Figure 12. Vertical displacement contours (m) in the dam core obtained from back-analysis of the end-of-construction (EOC) stage.

Table 8. Comparison between predicted and measured pore water pressure for two reservoir water elevations of 194 and 220 m.a.s.l.

instrument	Installation elevation	194 m.a.s.l.			220 m.a.s.l.		
		Vibrating wire piezometer reading pressure(kPa)	Model prediction pressure(kPa)	Relative Error Percentages	Vibrating wire piezometer reading pressure(kPa)	Model prediction pressure(kPa)	Relative Error Percentages
EP5-1	107.00	833.43	824.80	1.04	1009.40	1100.8	9.05
EP5-5	107.00	695.90	742.30	6.67	823.69	795.70	3.40
EP5-9	107.00	297.80	265.00	11.01	317.32	404.20	27.38
EP5-11	135.00	522.88	548.80	4.96	776.12	812.30	4.66
EP5-12	135.00	696.50	541.10	22.31	608.65	607.00	0.27
EP5-16	135.00	277.46	214.90	22.55	573.40	489.10	14.70
EP5-17	165.00	259.72	266.00	2.42	386.10	544.30	40.97
EP5-20	165.00	113.14	111.90	1.10	135.69	153.60	13.20
EP5-23	185.00	112.03	182.00	62.46	133.98	245.70	83.39
EP5-27	205.00	76.32	106.9	40.07	151.41	182.08	20.26

Table 9. Comparison between predicted and measured settlement for two reservoir water elevations of 194 and 220 m.a.s.l.

instrument	elevation	194 m.a.s.l.			220 m.a.s.l.		
		settlement gage reading (cm)	Model prediction settlement(cm)	Relative Error Percentages	settlement gage reading(cm)	Model prediction settlement(cm)	Relative Error Percentages
In5-2	128.790	89.999	47.9	46.78	-	49.3	-
	132.690	96.600	60.2	37.68	-	63.1	-
	139.960	106.474	72.7	31.72	-	75.5	-
	146.913	112.549	83.7	25.63	-	86.2	-
	150.785	115.600	92.9	19.64	-	95	-
	154.370	119.249	100.4	15.81	-	102.2	-
	161.663	124.274	106.4	14.38	-	108.8	-
	165.277	125.099	111.4	10.95	-	112.7	-
	172.432	126.850	117.1	7.69	-	117.9	-
	179.690	127.800	118.2	7.51	168.7	118.9	29.52
	183.339	128.900	115.9	10.09	170.975	116.3	31.98
	190.71	131.225	110.7	15.64	175.201	111.2	36.53
	198.096	133.349	103.4	22.46	178.724	104	41.81
	201.673	123.550	94.7	23.35	172.05	95.1	44.73
	208.84	100.649	85.0	15.55	147.599	84.8	42.55
	212.528	95.675	74.6	22.03	142.875	73.7	48.42
	216.172	86.324	64.6	25.17	133.725	62.5	53.26
	219.024	85.625	54.5	36.35	133.2	51.1	61.64
	222.764	78.475	44.8	42.91	126.601	40	68.40
	226.366	68.199	34.8	48.97	116.925	28.9	75.28
	229.932	53.800	25.3	52.97	102.701	18.8	81.69
	233.56	34.899	15.4	55.87	83.2	8.5	89.78

Table 10 presents the error metrics (RMSE, NRMSE, R^2, and MAE) between the model predictions and the measured values for two parameters: pore water pressure and dam body settlement, at two reservoir levels of 194 m.a.s.l. and 220 m.a.s.l. As evident from this table, the accuracy of the model is higher for the intermediate reservoir level compared to the normal water level. Specifically, while the model demonstrates relatively better agreement for pore water pressure across both elevations, it exhibits poor predictive performance for settlement as reflected by an R^2 of 0.04 at 194 m.a.s.l., and an RMSE of approximately 73 cm with a negative R^2 of -5.35 at 220 m.a.s.l. In other words, the practical engineering approach adopted in this study (calibrating the material parameters based on the maximum settlement and pore water pressure observed at the end-of-construction stage) results in higher prediction accuracy at intermediate reservoir levels and for pore water pressure. To achieve even greater accuracy, optimization algorithms could be employed to minimize errors across various reservoir stages. Such an approach would select a set of parameters that yields the lowest overall prediction error spanning from the minimum operating level to the normal water level. However, this specific optimization approach was not pursued in the current study. Additionally, the analyses conducted using FLAC in this study were performed under steady-state seepage conditions. However, Karkheh Dam reached its normal water level (220 m.a.s.l.) only once, specifically during a flood event. Under such rapid conditions, the formation of a fully developed steady state seepage flow network is practically impossible. Therefore, the transient nature of the actual field conditions compared to the steady state assumption in the numerical model may further explain the differences observed between the instrument readings and the model predictions at this specific reservoir level. Consequently, the inaccuracy in predicting static settlements at the 220 m.a.s.l. elevation directly impacts the subsequent dynamic MCE analysis performed at this reservoir level. Because the numerical model assumes a fully developed steady-state seepage condition at 220 m.a.s.l. (a condition that Karkheh Dam has never actually experienced during its 25-year operational history due to the transient, short-term nature of flood events at this level), the pre-earthquake stress state and pore pressure distribution carry inherent limitations. Therefore, the dynamic predictions under MCE loading at the 220 m.a.s.l. elevation

must be interpreted with clear recognition of these calibration uncertainties, rather than as absolute deterministic values.

Given that the dynamic analyses in this study were conducted at both 194 m.a.s.l. and 220 m.a.s.l. reservoir elevations, it can be concluded that the validity of the seismic evaluation is relatively higher for the 194 m.a.s.l. level. Furthermore, although 220 m.a.s.l. represents the normal water level, the reservoir reaches this elevation exclusively during flood events. The simultaneous occurrence of a major flood and a seismic event is highly improbable. Nevertheless, because standard dynamic analysis procedures for earth dams strictly require evaluation at the normal water level, the seismic analysis at the 220 m.a.s.l. elevation was performed and presented in this study to comply with conventional design practices.

Table 10. Normalized error metrics for pore water pressure and settlement at reservoir water elevations of 194 and 220 m.a.s.l.

Parameter	Pore Water Pressure		settlement	
reservoir water elevation	194 m.a.s.l.	220 m.a.s.l.	194 m.a.s.l.	220 m.a.s.l.
RMSE (Root Mean Square Error)	61.57 (kPa)	79.92(kPa)	25.70(cm)	73.11(cm)
NRMSE (Normalized Root Mean Square Error)	0.077	0.091	0.26	0.77
MAE (Mean Absolute Error)	43.98(kPa)	64.69(kPa)	24.12(cm)	72.21(cm)
Coefficient of Determination-R^2	0.94	0.92	0.04	-5.35

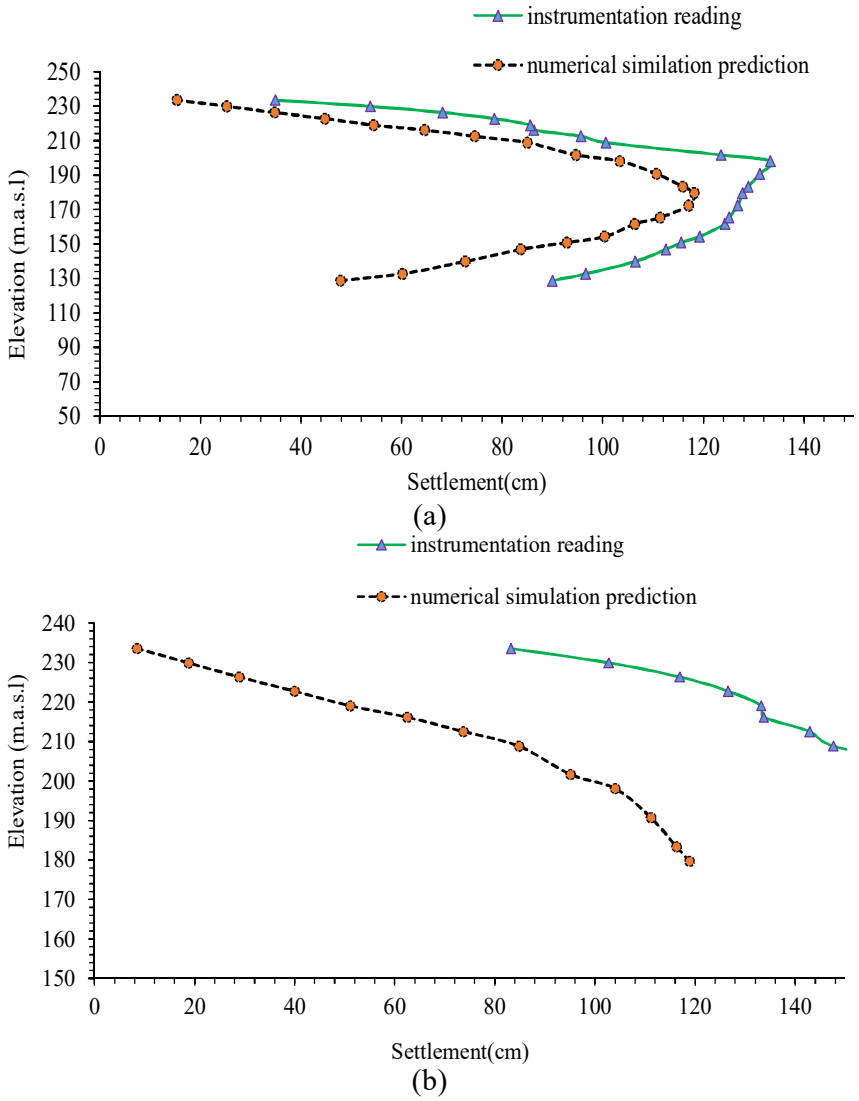

Figure 13. Comparison between monitored and simulated dam settlements at reservoir water elevations of (a) 194 m.a.s.l. and (b) 220 m.a.s.l.

Table 11. Parameters of dam zone materials after back-analysis.

zone	C (kPa)	Φ (^{0})	E (kPa)	k (cm/s)	γ (kN/m^3)
core	20	27	20000	2×10^{-8}	19
Filter and drain	0	35	20000	1×10^{-4}	20
shell	5	42	75000	1×10^{-3}	22

It is acknowledged that the constitutive model parameters were calibrated based on the available historical data and laboratory tests, which may not fully cover the extreme loading conditions imposed by the Maximum Credible Earthquake (MCE). Extrapolating these parameters to high-strain ranges introduces inevitable uncertainties regarding soil behavior. Consequently, the static calibration presented herein should be viewed as a baseline initialization rather than a validated dynamic response. However, to address these limitations qualitatively, standard empirical correlations as listed in Table 4 (e.g., Vucetic and Dobry, 1991; Seed and Idriss, 1970) were utilized to define the nonlinear behavior and stiffness degradation at larger strains. While this approach follows state-of-the-practice procedures, the predicted deformations under extreme loading should be interpreted with due consideration of these inherent uncertainties.

6.1. Sensitivity Analysis and Model Response

Although the dual variable calibration approach (simultaneously matching pore water pressures and maximum settlements) reduces parameter ambiguity during the back analysis procedure, a sensitivity analysis was conducted to evaluate the model behavior and sensitivity within the investigated ranges. To this end, a parameter screening process was first conducted to isolate the most governing variables and exclude non-contributing or physically constrained parameters.

Specifically, since the model calibration was strictly performed for the static end-of-construction phase, dynamic parameters such as the damping ratio were excluded from this sensitivity framework. Furthermore, the cohesion of the filter and drain zones is physically zero, and the shell material possesses merely negligible apparent cohesion (5 kPa); thus, their variations do not meaningfully affect the global static response. Similarly, the inherently high permeability of the shell, filter, and drain materials prevents the generation of excess pore water pressures in these zones, making the model insensitive to their hydraulic conductivity variations. Consequently, the sensitivity analysis was systematically focused on the key constitutive parameters of the core (shear strength, stiffness, and permeability) as well as the stiffness and friction angle of the shell, filter, and drain zones.

To evaluate model sensitivity, a One-At-a-Time (OAT) approach was adopted, where each selected parameter was varied independently while keeping the others constant. The baseline values for these parameters were initially extracted from the Phase II study report of the dam. The variation of in-situ soil parameters can be extensive. For instance, reported variations for the friction angle of sands range from 5% to 15%, while other parameters may exhibit variations between 12% and 56% [37]. However, it is a well-established premise that earthfill materials undergo rigorous quality control during construction; therefore, the actual range of variation for these compacted materials is significantly narrower than that of in-situ soils. Based on this engineering judgment, an approximate ±15% variation range around the baseline values was applied. It is emphasized that this ±15% range represents an investigation range based on practical engineering tolerances, rather than a statistical uncertainty interval or confidence range derived from site-specific stochastic testing of the Karkheh Dam.

The matrix of the sensitivity analysis scenarios and the corresponding effects on the end-of-construction responses are presented in Table 12. Accordingly, parameters that exhibited negligible influence within the evaluated ±15% variation range, specifically the hydraulic conductivity of the shell, filter, and drain zones, were excluded from Table 12 to maintain a concise presentation focused solely on the governing parameters. As demonstrated in this table, the maximum settlement is predominantly governed by the elastic modulus of the core and shell materials, whereas the excess pore water pressure is most sensitive to variations in the core permeability and, to a lesser extent, its shear strength.

Crucially, varying the baseline calibrated parameters independently by $\pm15\%$ leads to significant discrepancies between the numerical predictions and the target field measurements. It must be explicitly acknowledged that this One-At-a-Time (OAT) evaluation investigates local parameter responsiveness and stability within a practical operational bound. Consequently, it does

not capture potential multi-parameter coupling interactions, nor does it prove global optimality or uniqueness of the calibrated parameter set. Instead, the analysis serves to verify that the calibrated baseline configuration exhibits physically consistent and stable behavior under reasonable engineering perturbations, justifying its adoption for subsequent numerical phases while recognizing the inherent limitations of uncoupled univariate variation.

Table 12. Sensitivity analysis matrix and corresponding end-of-construction responses.

Sensitivity Analysis Scenario	Input Parameter Variation	Max. End-of-Construction Settlement (cm)	Max. Excess Pore Water Pressure (kPa)
Baseline Case (Calibrated)	Table11	120	695
Variations in core cohesion	C=15 kPa	120	700
	C=25 kPa	119	750
Variations in core friction angle	Φ=24^0	124	720
	Φ=31^0	116	685
Variations in core Elastic modulus	E=17000kPa	126.5	700
	E=23000kPa	108	700
Variations in core permeability	K=1.7×10^{-8} cm/s	118	800
	K=2.3×10^{-8} cm/s	121	665
Variations in filter and drain friction angle	Φ=30^0	121	695
	Φ=40^0	119	695
Variations in filter and drain Elastic modulus	E=17000kPa	122	695
	E=23000kPa	118.5	695
Variations in shell friction angle	Φ=37^0	123.5	695
	Φ=46^0	117	695
Variations in shell Elastic modulus	E=65000kPa	128	695
	E=86000kPa	113	695

7. Loading Conditions

For earth-rockfill dams with central clay cores, international experience gained from the construction of similar dams highlights several critical conditions and scenarios that must be considered in stability analyses [38-40]:

1. End-of-construction condition (before reservoir impoundment) — applicable to both upstream and downstream slopes.
2. Steady-state seepage condition (reservoir at normal water level) — applicable to the downstream slope.
3. Partial reservoir level condition — applicable to the upstream slope.
4. Rapid drawdown condition — applicable to the upstream slope.
5. Seismic loading — applied to scenarios 1, 2, and 3.

In the finite difference analysis, nonlinear dynamic simulations were conducted at two distinct reservoir elevations: the normal water level (220 m.a.s.l.) and a partial water level (194 m.a.s.l.). Additionally, the deformation of the dam was evaluated under an empty reservoir condition six years after the end-of-construction (EOC). It is important to note that reservoir levels at or above the 220 m.a.s.l. threshold are associated with extreme flood events, occurring exclusively under exceptional hydrological conditions with limited impoundment durations. Since combining seismic loading with such transient flood conditions does not represent a realistic or standard design scenario in geotechnical dam engineering, these critical states were evaluated separately. Consequently, for reservoir elevations exceeding the normal operating level, the analysis focuses exclusively on the static stability of the dam.

8. Limit Equilibrium Analysis

This section presents the stability analyses of the dam embankment using the limit equilibrium method under various probable loading conditions for the maximum cross-section of the dam. In the limit equilibrium approach, a potential sliding mass is first assumed, after which the driving and resisting forces are evaluated by solving the equilibrium equations. The resulting calculations yield the safety factor associated with the assumed sliding mass.

The stability analyses in this study were conducted using the method of slices, implemented in the SLOPE/W software. Both static and pseudo-static loading conditions were considered. The selected approach was the Morgenstern–Price technique, in which the inclination of the interslice resultant force relative to the horizontal is defined by a function with an associated coefficient. This coefficient is treated as an unknown and solved

within the system of equilibrium equations. The computed safety factors, along with the required design thresholds established by international standards, are summarized in Table 13. The loading conditions applied correspond to those anticipated during the dam's service life, as described in Section 7. To account for the hydraulic boundary conditions and pore water pressures within the limit equilibrium models, specific procedures were applied based on the loading scenarios. For the steady-state seepage and partial reservoir conditions, pore water pressure distributions and phreatic surfaces were initially computed using the SEEP/W software and subsequently imported into the SLOPE/W model. For the rapid drawdown scenario, a conservative approach was adopted to account for the low permeability of the clay core; the water level within the upstream shell was lowered to the minimum operating level, whereas the water table and corresponding pore pressures within the core were maintained at their pre-drawdown elevations. In addition to the normal reservoir levels, a scenario with a reservoir elevation exceeding the normal operating condition (227 m.a.s.l.) was analyzed under static loading, yielding a factor of safety of 1.79.

The critical slip surface corresponding to the minimum safety factor occurred under the pseudo-static downstream steady-state seepage condition (Figure 14). For pseudo-static analysis, applying the full unattenuated peak ground acceleration (PGA) is overly conservative because seismic acceleration is transient and non-directional. Following the established criteria of Marcuson (1981), the effective horizontal seismic coefficient for embankment dams is recommended to be taken as 33% to 50% of the PGA, paired with an acceptance criterion of FoS ≥ 1.00 [41]. In this study, the horizontal seismic coefficient was defined as 33% of the Maximum Credible Earthquake acceleration (kh = 0.33 × 0.645g = 0.213g).

Although the computed pseudo-static factors of safety (1.07 and 1.08) are slightly above unity, they comply with standard seismic design criteria (FoS ≥ 1.0). This acceptable margin is fully supported by the inherent conservatism of the pseudo-static approach, which replaces transient and cyclic seismic inertial forces with a sustained, unidirectional static load under the extreme Maximum Credible Earthquake (MCE) condition. As established by classical geotechnical frameworks, maintaining FoS ≥ 1.0 under such conservative assumptions confirms overall slope stability and ensures satisfactory seismic performance [42].

Table 13. Minimum factor of safety from limit equilibrium analyses (static and pseudo-static at the MCE level).

Loading condition	Slope	Water level (m.a.s.l.)	Static-Pseudo Static	Minimum safety factor	Allowable safety factor
Steady-state seepage	Downstream	220	Static	1.80	1.5 [40,43,44]
Steady-state seepage	Downstream	227	Static	1.79	
Partial reservoir level	Upstream	200	Static	1.99	1.5[45]
Rapid drawdown	Upstream	160	Static	2.14	1.1-1.3[40]
Steady-state seepage	Downstream	220	pseudo-static	1.07	1.0 [41,43,44,46,47]
Partial reservoir level	Upstream	210	pseudo-static	1.08	

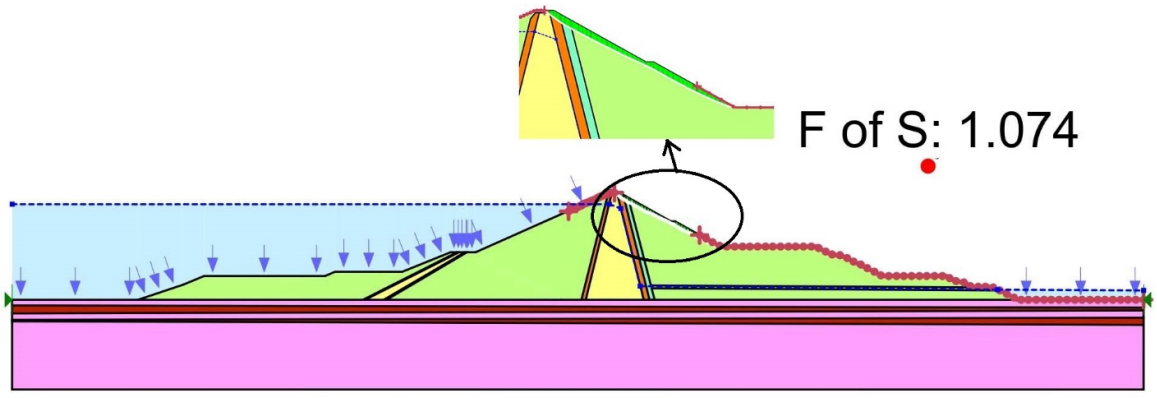

Figure 14. Critical slip surface of the downstream slope determined from pseudo-static analysis under steady-state seepage conditions (220 m.a.s.l.).

9. Dynamic Finite Difference Analysis

The results of horizontal and vertical displacements at different reservoir elevations under the T-Component of the Sarpol-e Zahab Earthquake are summarized in Table 14, while the displacement vector pattern is shown in Figure 15.

Figure 16 presents the vertical displacement distribution of the dam body at a reservoir water level of 220 m.a.s.l., indicating that the maximum settlement occurs at the dam crest. The contour lines at the end of the shaking are similar to those in previous studies [48].

As shown in Figure 17, the vertical stress distribution demonstrates the arching effect resulting from the contrast in elastic modulus between the core and shell materials, as established in prior analytical and numerical studies [7]. Under dynamic loading conditions, horizontal acceleration is amplified at the dam crest, as illustrated in Figure 18.

Table 14. Maximum post-earthquake residual horizontal and vertical displacements in the dam body at different reservoir water elevations under the T-component of the Sarpol-e Zahab earthquake at the MCE level.

Reservoir Water Elevation (m.a.s.l.)	Maximum Vertical Displacement (cm)	Maximum Horizontal Displacement (cm)
220	135	80
194	107	60

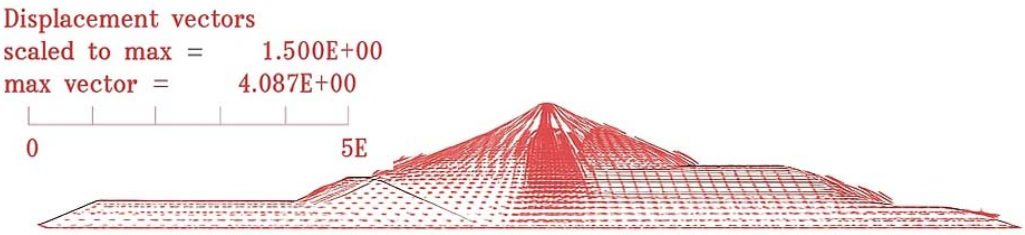

Figure 15. Displacement vector pattern induced by seismic excitation.

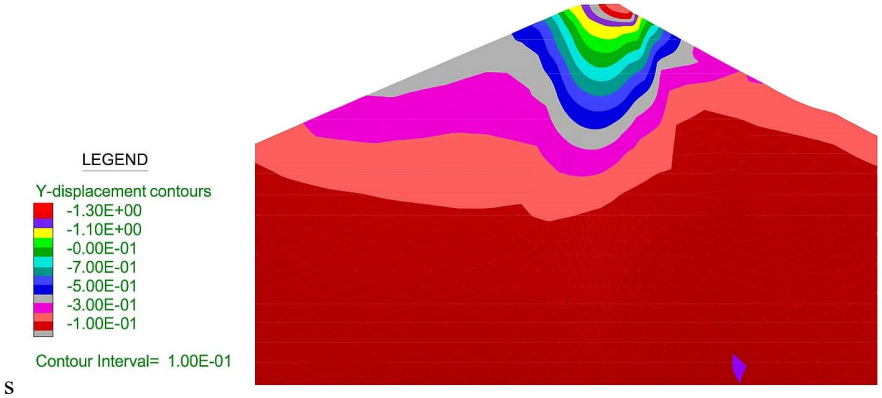

Figure 16. Vertical displacement pattern (in m) induced by the T-component of the Sarpol-e Zahab earthquake at the MCE level.

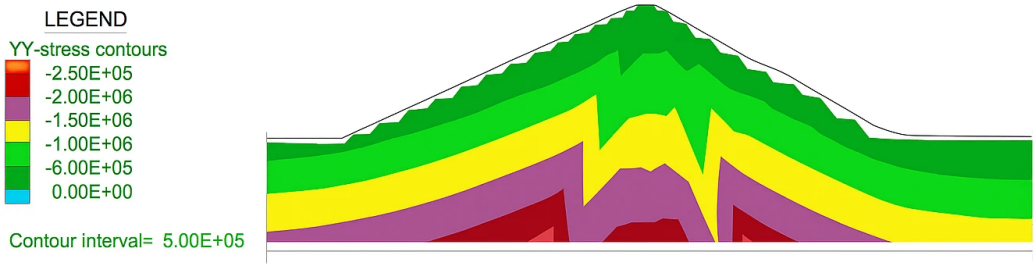

Figure 17. Vertical total stress distribution pattern (in Pa) induced by the T-component of the Sarpol-e Zahab earthquake at the MCE level.

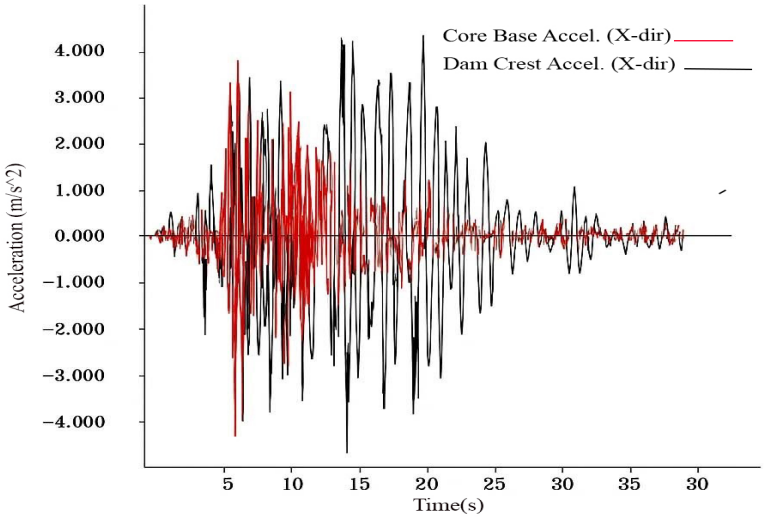

Figure 18. Amplification of horizontal acceleration time history at the dam crest.

10. Discussion and Conclusions

To assess the stability, dynamic response, and deformation magnitudes of the Karkheh Dam under updated seismic loading conditions, numerical analyses were performed. The limit equilibrium stability assessments yielded minimum factors of safety consistently above the required threshold of 1.0 under all loading scenarios, and no evidence of global instability was identified for the investigated loading scenarios within the limitations and assumptions of the adopted numerical framework (Table 13). Furthermore, dynamic time-history simulations indicated that predicted deformations under the maximum credible earthquake remain within acceptable limits and are well-distributed for the analyzed cases. Both the mean vertical settlements presented in Table 7 and the predicted maximum residual vertical crest displacement of 1.35 m (Figure 16) fall comfortably within the substantial 14 m freeboard, thereby significantly reducing the likelihood of overtopping under the specified ground motions. This magnitude of settlement is consistent with historical post-earthquake observations, which typically range between 1.2 and 1.8 meters [49], as well as the empirical limit of approximately 1.1% of the dam's height proposed by Hunter and Fell (2003) [50]. While global structural stability is indicated under these specific input motions, particular consideration must be given to internal zoning performance. The dam's exceptionally wide upstream (5 m) and downstream (6 m) filter zones are predicted to maintain substantial residual thickness following MCE-induced deformations. Although the initiation and progression of internal erosion were not explicitly modeled within the continuum deformation framework, this retained geometric continuity provides a favorable physical barrier to mitigate the potential migration of core materials under the analyzed loading conditions. It should be noted that the overall safety of the dam is not solely dependent on global stability safety factors and freeboard preservation. The risk of internal erosion resulting from seepage through the foundation and abutments of the Karkheh Dam has also been extensively investigated in prior studies [51]. Furthermore, factors such as cracking potential, filter performance, differential settlement, and post-seismic functionality play a critical role in the overall seismic assessment of the dam. Nevertheless, the probability of core cracking is continuously evaluated by analyzing data from piezometers located upstream and downstream of the core. Similarly, filter performance and differential settlements are closely monitored through the regular and continuous observation of the extensive instrumentation network installed within the dam body, allowing operators to evaluate and monitor the dam's behavior during and after seismic events. However, the comprehensive analysis and interpretation of such field instrumentation data remain outside the scope of the present numerical investigation.

The baseline conditions for these dynamic predictions were evaluated through back-analyses (Section 6). Calibrating the material properties to match the settlement and pore water pressures at the end-of-construction stage, and utilizing these parameters for subsequent analyses, proved to be a practical and simplified engineering approach in this study. However, it must be reiterated that this

static calibration serves strictly as a baseline initialization and does not constitute a direct validation of the dynamic constitutive response under cyclic loading. In contrast to recent seismic evaluations of large embankment dams that frequently rely on computationally expensive and highly complex optimization algorithms for long-term parameter calibration, the methodology employed here addresses a significant practical research gap. By anchoring the calibration strictly to the end-of-construction data, this approach bypasses the computational burden and uncertainties of simulating decades of transient seepage and consolidation. Consequently, it provides a streamlined and rapid preliminary framework specifically suited for the safety reassessment of aging earthfill dams. This methodology offers a practical alternative for bridging the gap between advanced numerical modeling and the practical time constraints of engineering projects, providing a cautious engineering approximation under maximum credible earthquake events, while explicitly distinguishing between the confidence levels at different operating stages. Specifically, while the model offers comparatively higher confidence for dynamic predictions at intermediate levels (194 m.a.s.l.), the predictions at the normal water level (220 m.a.s.l.) carry a significantly lower confidence level and higher uncertainty due to the statistical discrepancies identified during static back-analysis. Nevertheless, the proposed simplified framework provides these cautious approximations without the need for prohibitive computational resources.

While these practical insights provide a valuable reassessment framework, certain limitations highlight avenues for future research. Particularly, it must be noted that the analyses conducted in this study exclusively evaluate permanent deformations and cyclic strength degradation within the framework and limitations of the selected constitutive model (which does not explicitly capture cyclic pore-pressure generation using dedicated cyclic effective-stress formulations), and therefore cannot provide definitive conclusions regarding the non-occurrence of liquefaction, severe cyclic degradation, internal erosion initiation, or clay core cracking. Additionally, the designation of the Sarpol-e Zahab earthquake as the governing MCE scenario was based strictly on the maximum crest displacement criterion; thus, the possibility remains that other ground motions could be more critical for evaluating localized parameters such as internal stress concentrations or cracking. Furthermore, based on parametric studies conducted in previous research [52], the primary reliance on a 2D maximum cross-section model often oversimplifies geometric constraints and ignores the significant stabilizing effects of valley topography, the ratio of length to height, and the longitudinal arching effect. Moreover, in the context of dynamic analyses, investigations have shown that for earth dams where the ratio of crest length to height exceeds 4, the fundamental period obtained from 2D models provides a good approximation (with an error of less than 10%) compared to 3D models. However, even under these conditions, accelerations and dynamic stresses can exhibit significant differences between the two modeling approaches [53]. For the Karkheh Dam, the crest-length-to-height ratio is approximately 24, which is well above this threshold. However, this agreement primarily concerns the fundamental period as a selected dynamic characteristic and should not be interpreted as validation of the complete seismic response obtained from the 2D model. In particular, accelerations, dynamic stresses, strains, permanent deformations, and localized damage mechanisms may still exhibit significant differences between 2D and 3D modeling approaches. Therefore, the absence of a fully coupled 3D analysis represents an important limitation when interpreting spatial stress redistribution, longitudinal arching, differential deformation, and localized cracking or damage mechanisms. Future studies should incorporate advanced 3D coupled modeling to comprehensively capture these spatial effects.

From an operational and management perspective, this study underscores the critical need for a rigorous, continuous monitoring program throughout the dam's lifespan. Operators must maintain strict surveillance of seepage rates, pore water pressures, and crest settlements. Rather than serving as a deterministic trigger for the Emergency Action Plan (EAP), the predicted maximum crest displacement of 1.35 m under MCE conditions should be interpreted as a model-predicted reference deformation subject to numerical assumptions and analytical uncertainties. This reference value provides a benchmark to guide instrumentation thresholds, post-earthquake safety inspections, and operational decision-making. Finally, post-earthquake guidelines must mandate immediate, comprehensive inspections of the dam crest and filter zones to assess whether any transverse cracking or internal erosion has occurred, thereby

evaluating post-seismic operational performance and providing valuable long-term data to further refine numerical models.

References

[1]. Ahmed, T. M. (2025). Dynamic analysis of pore water pressure variation and stability in Earth dams during rapid and slow drawdown: Khassa Chai Earth dam as a case study. *Eurasian Journal of Science and Engineering*, 11(1), 11-23.

[2]. Hosseini, S., Mohammad, M., & Fard, R. A. (2003). Pore pressure development in the core of earth dams during simultaneous construction and impounding. *Electronic Journal of Geotechnical Engineering*, 8(1), 1-13.

[3]. Fu, J., Haeri, H., Sarfarazi, V., Wei, J., Fatehi Marji, M., & Golsanami, N. (2025). Numerical modeling of crack propagation patterns and the influence of joint configuration on tunnel and dam stability. *Computational Particle Mechanics*, 12, 5859–5881.

[4]. Haeri, H., Sarfarazi, V., Hedayat, A., & Zhu, Z. (2016). Numerical simulation of hydraulic fracturing in circular holes. *Computers and Concrete*, 18(6), 1135-1151.

[5]. Wu, Y., Yuan, H., Zhang, B., Zhang, Z., & Yu, Y. (2014). Displacement-based back-analysis of the model parameters of the Nuozhadu high Earth-rockfill dam. *The Scientific World Journal*, 2014(1), 292450.

[6]. Farajniya, R., Poursorkhabi, R. V., Zarean, A., & Dabiri, R. (2024). Analysis and monitoring of the behavior of a rock fill dam ten years after construction: a case study of the Iran-Madani Dam. *Geoenvironmental Disasters*, 11(1), 30.

[7]. Rashidi, M., & Haeri, S. M. (2017). Evaluation of behaviors of earth and rockfill dams during construction and initial impounding using instrumentation data and numerical modeling. *Journal of Rock Mechanics and Geotechnical Engineering*, 9(4), 709-725.

[8]. Su, H., Wen, Z., Zhang, S., & Tian, S. (2016). Method for choosing the optimal resource in back-analysis for multiple material parameters of a dam and its foundation. *Journal of Computing in Civil Engineering*, 30(4), 04015060.

[9]. Jeon, Y., & Yang, H. (2004). Development of a back analysis algorithm using FLAC. *International Journal of Rock Mechanics and Mining Sciences*, 41, 447-453.

[10]. Scaioni, M., Marsella, M., Crosetto, M., Tornatore, V., & Wang, J. (2018). Geodetic and remote-sensing sensors for dam deformation monitoring. *Sensors*, 18(11), 3682.

[11]. Ghiasi, V., Heydari, F., & Behzadinezhad, H. (2021). Numerical analysis and back calculation for embankment dam based on monitoring results (Case study: Iran-Lurestan Rudbar). *Scientia Iranica*, 28(5), 2519-2533.

[12]. Haeri, H., Tavakoli, H., Shemirani, A., Sarfarazi, V., & Farazmand, M. (2016). Evaluating the use of mineral pumice in falling zones of internal pressure tunnels (Case study: Water transfer tunnel of Sardasht dam power plant). *Journal of Mining Science*, 52(6), 1060-1068.

[13]. Lei, Z., Jafari, Z., Sarfarazi, V., Haeri, H., Moarefvand, P., Fatehi Marji, M., & Faghihimohammadi, S. (2022). PLAXIS 3D simulation, FLAC3D analysis and in situ monitoring of Excavation stability. *Structural Engineering and Mechanics: An International Journal*, 84(6), 743-765.

[14]. Sarayli, S., Sert, S., & Sonmez, O. (2024). Analysis of Fill Dam Using Finite Element Method and Comparison with Monitoring Results. *Water*, 16(17), 2387.

[15]. Yaseen, Z. M., Al-Hetari, M., & Ali, U. (2025). Earth and Rockfill Dams' Seepage Prediction Using Artificial Intelligence Models: A Comprehensive Review Assessment, and Future Research Directions. *Archives of Computational Methods in Engineering*, 33, 4755–4791.

[16]. Zhang, H., Song, Z., Sun, Y., Ding, Z., Zhang, X., Han, P., & Ma, C. (2022). Back-analysis of dynamic property of earth-rock dam considering parameter uncertainly. *Arabian Journal of Geosciences*, 15(23), 1712.

[17]. Kamalzare, M., & Marquez, H. (2020). Stability Assessment of the Embankment Dam Systems Under Different Seismic Loads in Southern California and Evaluation of the Current Design Criteria. *The International Conference on Embankment Dams*, 163-174.

[18]. Javdanian, H., Zarei, M., & Shams, G. (2023). Estimating seismic slope displacements of embankment dams using statistical analysis and numerical modeling. *Modeling Earth Systems and Environment*, 9(1), 389-396.

[19]. Kontoe, S., Zdravković, L., Han, B., & Pelecanos, L. (2019). Hydrodynamic effects and hydro-mechanical coupling in the seismic response of dams. In *Earthquake Geotechnical Engineering for Protection and Development of Environment and Constructions* (pp. 506-521). Rome, Italy: CRC Press.

[20]. Ghaderi, A., Nazari, F., & Mohammadnezhad, H. (2026). Hydro-Mechanical Response of an Earth-Fill Dam During Rapid Reservoir Drawdown Using Coupled Seepage and Stability Analysis. *Geotechnical and Geological Engineering*, 44(3), 187.

[21]. Casablanca, O., Di Filippo, G., Giretti, D., Masini, L., Rollo, F., & Tretola, M. (2024). Coupled hydro-mechanical modelling of the seismic response of a zoned earth dam. *Japanese Geotechnical Society Special Publication*, 10(13), 366-371.

[22]. Tretola, M., Coppola, L., Sica, S., & Pagano, L. (2026). Seismic analysis of a zoned earth dam after decades of operation. *Engineering Geology*, 363, 108559.

[23]. Mahin Roosta, R., & Tabibnejad, A. (2005). Back analyses of Maroon embankment dam. Paper presented at the *Proceedings of the 16th International Conference on Soil Mechanics and Geotechnical Engineering (16th ICSMGE)*, Osaka, Japan.

[24]. American Society of Civil Engineers. (2017). *Minimum Design Loads and Associated Criteria for Buildings and Other Structures* (ASCE Standard ASCE/SEI 7-16). Reston, VA: American Society of Civil Engineers.

[25]. Psaroudakis, E., & Klimis, N. (2026). Numerical simulation of a rockfill dam subjected to consecutive earthquakes: total and effective stress analysis versus recorded field data. *Soil Dynamics and Earthquake Engineering*, 208, 110376.

[26]. Board, M. (1989). *FLAC (Fast Lagrangian Analysis of Continua) Version 2.20: Software summary* (NUREG/CR-5430). Washington, DC: U.S. Nuclear Regulatory Commission, Division of High-Level Waste Management.

[27]. Loprevite, L. (2021). *Stress-deformation analysis of a zoned earth dam with elasto-plastic hardening soil models* (Master's thesis). Politecnico di Torino, Turin, Italy.

[28]. Huang, J., & Romanel, C. (2020). *Implementation of a Single Hardening Constitutive Model for 3D Analysis of Earth Dams*. Cham, Switzerland: Springer.

[29]. Sukkarak, R., Likitlersuang, S., Jongpradist, P., & Jamsawang, P. (2021). Strength and stiffness parameters for hardening soil model of rockfill materials. *Soils and Foundations*, 61(6), 1597-1614.

[30]. Hardin, B. O., & Drnevich, V. P. (1972). Shear modulus and damping in soils: design equations and curves. *Journal of the Soil Mechanics and Foundations Division*, 98(7), 667-692.

[31]. Zhang, J., Andrus, R. D., & Juang, C. H. (2005). Normalized shear modulus and material damping ratio relationships. *Journal of Geotechnical and Geoenvironmental Engineering*, 131(4), 453-464.

[32]. Vucetic, M., & Dobry, R. (1991). Effect of soil plasticity on cyclic response. *Journal of Geotechnical Engineering*, 117(1), 89-107.

[33]. Hardin, B. O., & Black, W. L. (1968). Vibration modulus of normally consolidated clay. *Journal of the Soil Mechanics and Foundations Division*, 94(2), 353-369.

[34]. Kokusho, T., & Esashi, Y. (1981). Cyclic triaxial test on sands and coarse materials. Paper presented at the *Proceedings of the 10th international conference on soil mechanics and foundation engineering*, Stockholm, Sweden.

[35]. Seed, H. B. (1970). *Soil moduli and damping factors for dynamic response analyses* (EERC 70-10). Berkeley, CA: Earthquake Engineering Research Center, University of California.

[36]. International Commission on Large Dams. (2010). *Selecting Seismic Parameters for Large Dams, Guidelines* (Bulletin 148). Paris: ICOLD.

[37]. Christian, J. T., & Baecher, G. B. (2003). *Reliability and Statistics in Geotechnical Engineering* (Vol. 182). Chichester / New York: John Wiley & Sons.

[38]. Gebrehiwot, M. (2020). *Analysis of seepage and slope stability in embankment dam: Case of Mhtsab Azmat earthen dam, Central Tigray, Ethiopia* (Master's thesis). School of Civil Engineering, Mekelle University, Ethiopia.

[39]. Fell, R., MacGregor, P., Stapledon, D., Bell, G., & Foster, M. (2014). *Geotechnical Engineering of Dams* (2nd ed.). London: CRC Press / Balkema.

[40]. U.S. Army Corps of Engineers. (2003). *Slope Stability*. Washington, DC: U.S. Army Corps of Engineers.

[41]. Marcuson, W. (1981). Moderator's report for session on earth dams and stability of slopes under dynamic loads. Paper presented at the *Proc., Int. Conf. on recent adv. In Geotech. Earthquake Engrg. And Soil Dyn.*, Univ. of Missouri.

[42]. Hynes-Griffin, M. E. (1984). *Rationalizing the seismic coefficient method* (Miscellaneous Paper GL-84-13). US Army Corps of Engineers.

[43]. Canadian Dam Association. (2007). *Canadian Dam Safety Guidelines*. Edmonton, AB, Canada: Canadian Dam Association (CDA).

[44]. Federal Energy Regulatory Commission. (1991). *Embankment Dams* (Engineering Guidelines for the Evaluation of Hydropower Projects, Chapter IV). Washington, DC: Federal Energy Regulatory Commission (FERC), Division of Dam Safety and Inspections.

[45]. Sharma, H. D. (1991). *Embankment dams*. New Delhi: Oxford & IBH Publishing Company.

[46]. National Research Council. (1985). *Safety of dams: flood and earthquake criteria*. Washington, DC: The National Academies Press.

[47]. Federal Emergency Management Agency. (2013). *The National Dam Safety Program Research Needs Workshop: Embankment Dam Failure Analysis*. Washington, DC: Createspace Independent Publishing Platform.

[48]. Elia, G., Amorosi, A., Chan, A. H., & Kavvadas, M. J. (2011). Numerical prediction of the dynamic behavior of two earth dams in Italy using a fully coupled nonlinear approach. *International Journal of Geomechanics*, 11(6), 504-518.

[49]. Seed, H. B., Makdisi, F. I., & De Alba, P. (1978). Performance of earth dams during earthquakes. *Journal of the Geotechnical Engineering Division*, 104(7), 967-994.

[50]. Hunter, G., & Fell, R. (2003). *The deformation behaviour of embankment dams* (UNICIV Report No. R-416). Sydney, Australia: School of Civil and Environmental Engineering, The University of New South Wales.

[51]. Salehinik, M., Mirghasemi, A. A., & Tabibnejad, A. (2026). Three-Dimensional Seepage Back Analysis of Dam Foundation and Abutments: a Case Study of the Karkheh Dam. *Rudarsko-geološko-naftni zbornik*, 41(4), in press.

[52]. Yu, Y., Xie, L., & Zhang, B. (2005). Stability of earth–rockfill dams: influence of geometry on the three-dimensional effect. *Computers and Geotechnics*, 32(5), 326-339.

[53]. Mejia, L. H., & Seed, H. B. (1983). Comparison of 2-D and 3-D dynamic analyses of earth dams. *Journal of Geotechnical Engineering*, 109(11), 1383-1398.

انجمن مهندسی معدن ایران
نشریه مهندسی معدن و محیط زیست
نشانی نشریه: www.jme.shahroodut.ac.ir
دانشگاه صنعتی شاهرود

ارزیابی ایمنی سد خاکی با استفاده از تحلیل برگشتی؛ مطالعه موردی سد کرخه

محمد صالحی‌نیک[1] و حسن سرفراز[2*]

۱. دانشکده مهندسی عمران، پردیس دانشکده‌های فنی، دانشگاه تهران، تهران، ایران
۲. دانشکده مهندسی معدن، پردیس دانشکده‌های فنی، دانشگاه تهران، تهران، ایران

اطلاعات مقاله

تاریخ ارسال: ۲۰۲۶/۰۴/۲۵
تاریخ داوری: ۲۰۲۶/۰۹/۳۰
تاریخ پذیرش: ۲۰۲۶/۱۰/۰۶

DOI: 10.22044/jme.2026.17639.3504

کلمات کلیدی

تحلیل برگشتی
ارزیابی ایمنی سد
رفتارنگاری
سد کرخه
مدلسازی عددی

چکیده

سد کرخه، سدی خاکی با هسته رسی مرکزی و ارتفاع ۱۲۷ متر در ایران است که با گنجایش ۵/۹ میلیارد متر مکعب، بزرگ‌ترین مخزن کشور را تشکیل می‌دهد. در فروردین ۱۳۹۸، تراز آب مخزن افزایشی بی‌سابقه به میزان ۵ متر بالاتر از تراز بهره‌برداری نرمال را تجربه نمود که این امر، نگرانی‌هایی را در خصوص پایداری بلندمدت سد تحت شرایط ماندابی در ترازهای بالای آب برانگیخت. به منظور پاسخ به این دغدغه‌ها، ارزیابی ایمنی جامعی با تلفیق تحلیل داده‌های ابزاردقیق، تحلیل‌های تعادل حدی با نرم‌افزار SLOPE/W، و تحلیل برگشتی عددی به همراه شبیه‌سازی‌های دینامیکی غیرخطی با نرم‌افزار FLAC و با اعمال نگاشت‌های لرزه‌ای به‌روزرسانی‌شده ویژه ساختگاه انجام پذیرفت. مدل عددی به صورت تکرارشونده بر اساس تغییرشکل‌ها و فشارهای آب حفره‌ای مشاهداتی واسنجی گردید تا بازتاب درستی از رفتار واقعی سد حاصل شود. اگرچه روش به کارگرفته شده، تقریب‌های کاربردی مناسبی را برای ترازهای میانی مخزن به دست می‌دهد، ارزیابی‌های آماری نشان می‌دهند که پیش‌بینی‌ها در تراز آب نرمال ۲۲۰ متر بالاتر از سطح دریا، از عدم قطعیت بیشتر و سطح اطمینان کمتری برخوردارند. با این وجود، در چارچوب محدودیت‌های این مدل‌سازی ساده‌شده، نتایج حاکی از آن است که سد تحت سناریوهای بارگذاری استاتیکی و لرزه‌ای بررسی‌شده، پایداری رضایت‌بخشی دارد. تحت اثر زلزله حداکثر محتمل وقوع، بیشینه تغییرمکان ماندگار محاسبه‌شده در تحلیل‌ها حدود ۱/۳۵ متر برآورد می‌شود. با توجه به ارتفاع آزاد قابل‌توجه سد به میزان ۱۴ متر، این تغییرشکل نشان‌دهنده ریسک بسیار ناچیز وقوع روگذری است. افزون بر این، تحلیل‌ها تأیید می‌کنند که زون‌های فیلتر بالادست و پایین‌دست به پهنای ۵ تا ۶ متر، پس از تغییرشکل‌های لرزه‌ای، ضخامت باقیمانده کافی را به منظور جلوگیری از بروز فرسایش داخلی حفظ می‌نمایند. در نتیجه، در محدوده فرضیات و محدودیت‌های روش عددی به‌کاررفته، هیچ نشانه‌ای مبنی بر ناپایداری کلی یا روگذری آب از تاج سد در سناریوهای بارگذاری بررسی‌شده مشاهده نگردید.

نویسنده مسئول مکاتبات: Sarfaraz @ut.ac.ir (ح. سرفراز)